JOURNAL OF GEOPHYSICAL RESEARCH, VOL. 114, B02305, doi:10.1029/2008JB005856, 2009

Crustal structure of the Hatton and the conjugate east Greenland rifted volcanic continental margins, NE Atlantic

Robert S. White[1] and Lindsey K. Smith[1,2]

Received 6 June 2008; revised 28 October 2008; accepted 12 November 2008; published 13 February 2009.

[1] We show new crustal models of the Hatton continental margin in the NE Atlantic using wide-angle arrivals from 89 four-component ocean bottom seismometers deployed along a 450 km dip and a 100 km strike profile. We interpret prominent asymmetry between the Hatton and the conjugate Greenland margins as caused by asymmetry in the initial continental stretching and thinning, as ubiquitously observed on ''nonvolcanic'' margins elsewhere. This stretched continental terrain was intruded and flooded by voluminous igneous activity which accompanied continental breakup. The velocity structure of the Hatton flank of the rift has a narrow continent-ocean transition (COT) only ~40 km wide, with high velocities (6.9–7.3 km/s) in the lower crust intermediate between those of the continental Hatton Bank on one side and the oldest oceanic crust on the other. The high velocities are interpreted as due to intrusion of igneous sills which accompanied the extrusion of flood basalts at the time of continental breakup. The variation of thickness (h) and P wave velocities (v_p) of the igneous section of the COT and the adjacent oceanic crust are consistent with melt formation from a mantle plume with a temperature ~120–130°C above normal at breakup, followed by a decrease of ~70–80°C over the first 10 Ma of seafloor spreading. The h-v_p systematics are consistent with the dominant control on melt production being elevated mantle temperatures, with no requirement for either significant active small-scale mantle convection under the rift or of the presence of significant volumes of volatiles or fertile mantle.

Citation: White, R. S., and L. K. Smith (2009), Crustal structure of the Hatton and the conjugate east Greenland rifted volcanic continental margins, NE Atlantic, *J. Geophys. Res.*, *114*, B02305, doi:10.1029/2008JB005856.

1. Introduction

[2] The description of some continental margins as ''volcanic'' is intended to convey the fact that continental breakup was accompanied by the eruption of huge volumes of basaltic lavas. Such margins stand in distinction to nonvolcanic margins that exhibit only minor, or restricted igneous activity at the time of continental breakup. In one sense the distinction between volcanic and nonvolcanic margins is unhelpful because there is some igneous activity on all rifted margins; indeed, by the time that seafloor spreading has started, the crust adjacent to all rifted margins is 100% igneous, as it generates oceanic crust. But the volcanic versus nonvolcanic distinction remains useful in places like the northern North Atlantic, where continental breakup between Greenland and northwest Europe was accompanied by the production of large volumes of flood basalts which flowed across the continental hinterlands on both sides of the new ocean basin. In the case of the northern North Atlantic, the volume of the extrusive lavas reached more than 1×10^6 km^3 [*White and McKenzie*, 1989; *Coffin and Eldholm*, 1994; *Eldholm and Grue*, 1994], with at least as much again intruded as igneous rocks into the lower crust on the continent-ocean transition [*White et al.*, 2008].

[3] The northern North Atlantic can be considered as the type example of volcanic rifted margins. There have been extensive studies of the continental margins on both sides of the North Atlantic, particularly using seismic methods and by drilling (DSDP leg 12 [*Laughton et al.*, 1972]; DSDP leg 81 [*Roberts et al.*, 1984]; ODP leg 152 [*Saunders et al.*, 1998]; ODP leg 163 [*Larsen et al.*, 1999]). This means that there are now several studies of the continental margins in approximately conjugate locations on either side of the ocean basin [e.g., *Hopper et al.*, 2003; *Smith et al.*, 2005; *Voss and Jokat*, 2007]. In this paper we report new crustal structure results from a pair of strike and dip profiles with dense deployments of ocean bottom seismometers (OBS) across the Hatton Bank margin west of Rockall (Figure 1) that provide control on the structure from wide-angle data with unprecedented density and number of arrivals. The Hatton profile is approximately conjugate to the SIGMA-3 profile across the Greenland continental margin [*Holbrook et al.*, 2001; *Korenaga et al.*, 2002; *Hopper et al.*, 2003]. Both the Greenland and Hatton Bank profiles extend more than 150 km across the adjacent oceanic crust, so provide an opportunity to map the structure from the continental block, across the continent-ocean transition (COT) and into oceanic crust formed by mature seafloor spreading. Comparison of the Hatton Bank structure from previous seismic studies

[1]Bullard Laboratories, University of Cambridge, Cambridge, UK.
[2]Now at BP, Aberdeen, UK.

0148-0227/09/2008JB005856$09.00

made in the late 1980s [*White et al.*, 1987; *Spence et al.*, 1989; *Fowler et al.*, 1989; *Morgan et al.*, 1989] with the conjugate Greenland structure show marked asymmetry [*Hopper et al.*, 2003; *Smith et al.*, 2005]. Similar asymmetry has been reported from conjugate margins north of Iceland [*Voss and Jokat*, 2007]. In this paper we report recent, detailed studies of the Hatton margin and then examine the nature of this asymmetry with the conjugate margin and discuss possible causes for it.

[4] When volcanic continental margins were first studied in detail, it became apparent that the widespread extrusive volcanics were invariably accompanied by high-velocity lower crust (HVLC, P wave velocities higher than 7.0 km/s) beneath the continent-ocean transition. This was generally interpreted as due to ''underplated'' igneous crust [e.g., *Mutter et al.*, 1984; *LASE Study Group*, 1986; *Vogt et al.*, 1998; *Klingelhöfer at al.*, 2005; *Voss and Jokat*, 2007]. Recent high-quality seismic reflection profiles across the Faroes continental margin show the presence of numerous lower crustal sills beneath the COT, so the high-velocity lower crust is better interpreted as ''intruded lower crust'' than as underplated igneous crust [*White et al.*, 2008]. On the Hatton margin studied here we do not have available a deep penetration seismic reflection profile such as that on the Faroes margin which made it possible to image the lower crustal sills there. However, *White et al.* [2008] showed that the architecture of the high-velocity lower crust on the COT of the Faroes margin is almost identical to the velocity structure of the COT portion of the long Hatton dip line that we report in more detail in this paper (compare Figure 7a with Figure 2b of *White et al.* [2008]). This gives us confidence to interpret the HVLC on the Hatton margin as also caused by igneous sills intruded into stretched continental crust. In this paper we also report results from a hitherto unpublished strike profile which is located above the thickest part of the HVLC and provides better control on its velocity than does the dip line, because unlike the dip profile, the strike profile crosses only limited lateral variations in structure. As we discuss later, the widespread use of the terminology of underplated igneous crust rather than intruded lower crust makes a significant, and we aver sometimes erroneous difference to the way the cause of the widespread magmatism is interpreted.

2. Survey Data

[5] A total of 89 four-component ocean bottom seismometers was deployed along three profiles in the area of the Hatton Bank rifted continental margin (Figure 1). The main 450 km dip line runs along a great circle across the continental margin, starting in the stretched continental crust of the Mesozoic Hatton Basin, across the continental block of Hatton Bank and the COT, and 150 km into the oceanic crust of the Iceland Basin (Figure 2). The main 175-km-long strike line is perpendicular to the dip line, located above the thickest expression of the high-velocity lower crust on the COT. The intersection point of the two profile lines is ~30 km along strike from the center of the Hatton survey lines shot in 1985 (Figure 1), and results from that work [*White et al.*, 1987; *Spence et al.*, 1989; *Fowler et al.*, 1989; *Morgan et al.*, 1989] were used to optimize the location of the dip line. A second 100-km-long strike line was located over 43 Ma oceanic crust [*Parkin and White*, 2008] and will not be discussed further here.

[6] The OBS were spaced 4 km apart in the vicinity of the intersection of the main dip and strike lines, with the spacing increased to 10 km elsewhere (circles, Figure 1). All the OBS were provided by Geopro, and comprised a hydrophone with a gimballed type SM-6, 4.5 Hz three-component geophone. Data were recorded digitally at 4 ms sample rate using a 24-bit analog-digital converter with 120 dB dynamic range. Although the weather deteriorated at times to Force 7 during shooting, noise on the OBS remained low throughout, with strong arrivals recorded typically to ranges of more than 100 km.

[7] A vertical hydrophone array was deployed at the intersection point of the dip and strike lines (Figure 1), and used to calculate the waveform of the air gun source [*Lunnon et al.*, 2003]. In order to produce a low-frequency, high-amplitude source capable of propagating long distances through the basalts, which severely attenuate high-frequency energy [*Maresh and White*, 2005], we deployed a 14-gun array totaling 104 L (6360 in^3), towed at 20 m depth, which generated a waveform centered on 9–10 Hz [*White et al.*, 2002]. Shots were fired at 150 m intervals, giving approximately 60 s between successive shots to avoid contamination of the wide-angle arrivals by wraparound of seabed multiples from previous shots [*McBride et al.*, 1994].

[8] A multichannel seismic (MCS) reflection profile was recorded simultaneously with the OBS profile, using a 2400 m long, 96 channel streamer towed at 20 m depth. The sparse shot interval means that the maximum fold of cover was 8. The MCS profiles were used primarily to map the sediment thickness and seismic velocity down to the top of the basement along the profiles, which were used subsequently in the starting models for tomographic inversion of the wide-angle arrival traveltimes. Water depths along the profiles were measured using both 3.5 kHz and 10 kHz echo sounders, and the water velocity profile determined from a velocimeter dip and by deploying expendable bathythermographs (XBTs) along the profiles. The magnetic field was recorded using a towed proton precession magnetometer, from which seafloor spreading magnetic anomalies were identified.

3. Wide-Angle (OBS) Data Processing

[9] The main focus of this paper is the crustal structure derived from traveltime tomography of the wide-angle diving waves and reflections recorded on the OBS. The first stage in data reduction was to apply a clock-drift correction to the internal OBS clocks, assuming a constant drift rate between the clock calibrations that were made immediately before deployment and after recovery: the average OBS clock drift rate was ~12 ms/d. Next we calculated the positions of the OBSs, as some instruments drifted to an average of 400 m offline as they sank. For most of the OBS we used the direct water wave traveltime at the point of closest approach, together with the water wave acoustic velocity derived from the velocimeter dip and XBTs. For the 2-D tomographic inversion programs, we assumed that the OBS were positioned on the profiles at the points of closest approach. The traveltime errors introduced by this procedure are less than 4 ms (i.e., less than one sample) for basalt or basement arrivals at offsets greater than 4 km, so are small compared to picking uncertainties. For the

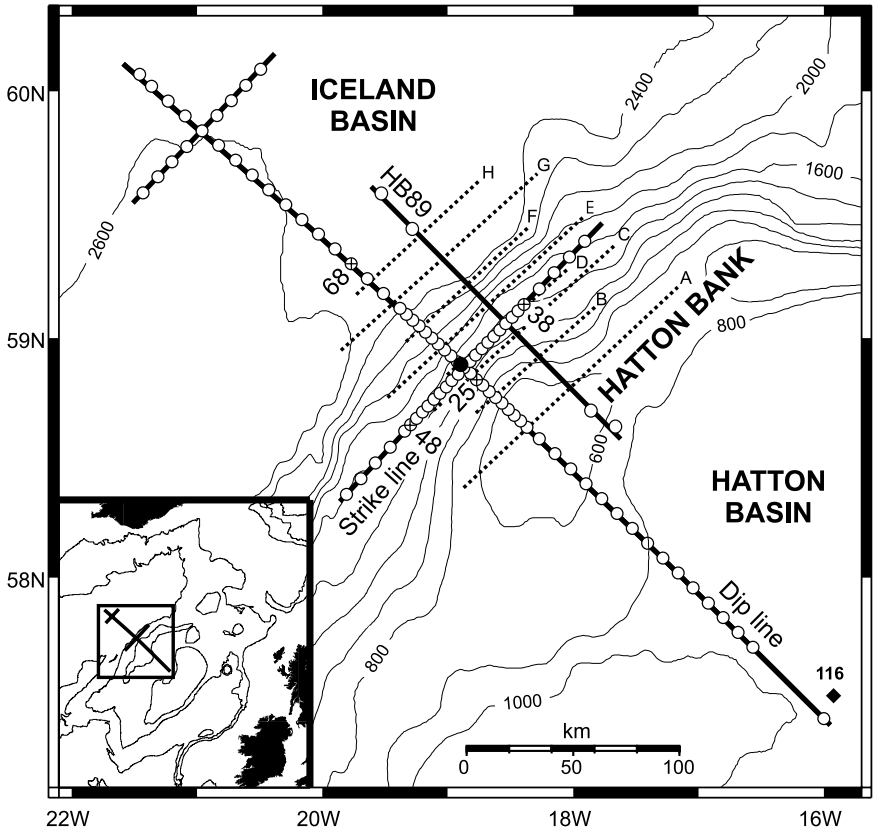

Figure 1. Layout of normal incidence and wide-angle seismic profiles and ocean bottom seismometer locations (open circles) for the experiment reported here. Example record sections from OBS numbered and marked by crosses inside the circles are shown in Figures 3 and 4. HB89 is location of earlier wide-angle profile reported by *Morgan et al.* [1989] and shown in Figure 9b. Dotted profiles labeled A–H perpendicular to this show locations of expanding spread profiles used to constrain the dip line structure by *White et al.* [1987], *Fowler et al.* [1989], and *Spence et al.* [1989] and shown in Figure 9a. DSDP drill site 116 is shown by diamond. Filled circle at intersection of strike and dip lines shows location of vertical hydrophone array used to calculate air gun source waveform. Contours in meters, interval 200 m.

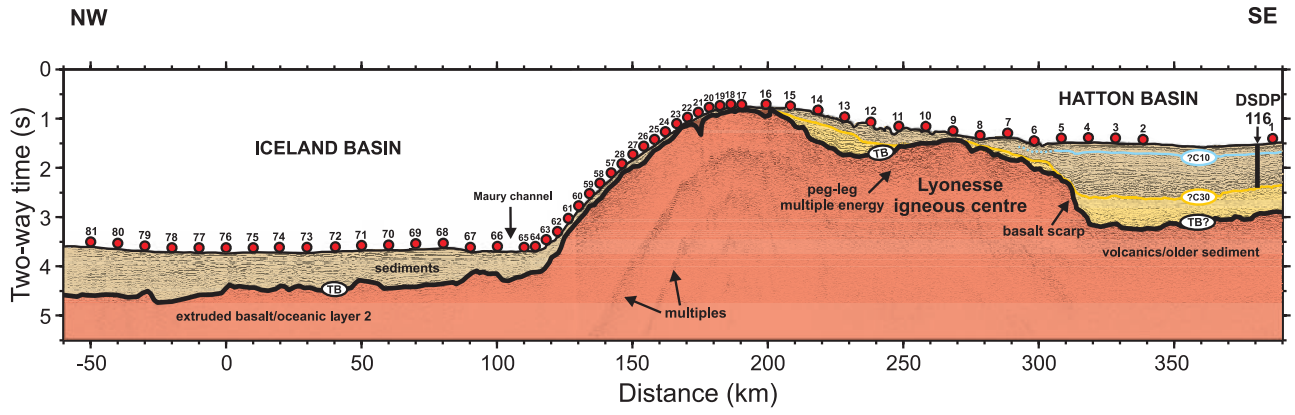

Figure 2. Multichannel seismic reflection profile along dip line showing locations and numbering of OBSs and intersection point with main strike line. TB marks top basalt horizon, C30 and C10 mark regional unconformities in Hatton Basin that can be correlated with identical unconformities in Rockall Basin [*Hitchen*, 2004]. DSDP hole 116 [*Laughton et al.*, 1972] is projected onto the profile from its location 11 km to the northeast (see Figure 1).

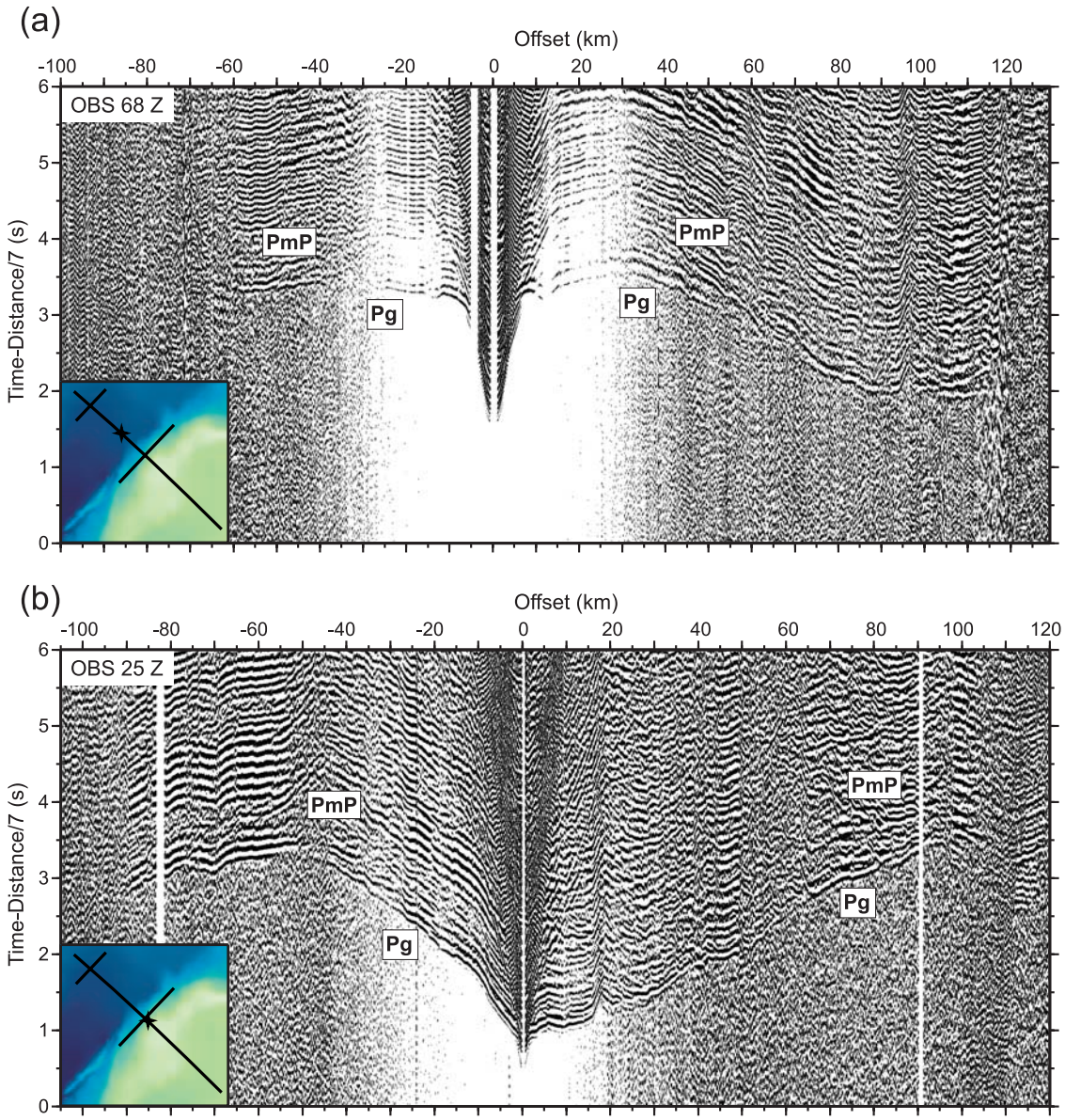

Figure 3. Examples of vertical geophone recordings of wide-angle seismic data from the dip line: (a) OBS 68, over oceanic crust in the Iceland Basin. (b) OBS 25, over continental crust of Hatton Bank (see Figures 1 and 2 for location). Traces are scaled to a common maximum amplitude, band-pass-filtered 2–15 Hz, with traveltimes reduced at 7 km/s. Stars on inset show locations of OBS (see also Figures 1 and 2).

sediment velocities, we used semblance analysis on the coincident MCS profile, so they are unaffected by these errors.

[10] No further processing was applied to the OBS data, other than demeaning to remove a DC shift and application of a 2–15 Hz zero-phase filter to attenuate noise. Examples of receiver gathers from two OBS on the dip line (Figure 3) and two on the strike line (Figure 4) demonstrate the quality of the arrivals. Plots of all the OBS receiver gathers are shown in the auxiliary material.[1] Two OBS in the Maury Channel at the foot of the continental slope (Figure 2) were consistently noisier than other OBS, presumably due to water currents, but other than those it was possible to pick crustal diving phases Pg and Moho reflections PmP from almost all the OBS. This produced a data set of 39,303 Pg and 10,008 PmP traveltimes on the dip and strike lines combined. Mantle refractions, Pn, were apparent on only some of the OBS (e.g., Figure 4b). In general, the arrivals were more consistent between adjacent OBS on the strike line with its limited lateral variability than on the dip line which crosses all the major structure created during continental breakup. Uncertainties in the traveltimes were assessed for each arrival pick, according to the signal-to-noise ratio, varying in five steps from 20 ms for the best arrivals to 120 ms for the poorest, where it was possible that the correct first arriving phase had been missed, resulting in a cycle skip. Reciprocity tests were made to check the consistency of traveltimes between pairs

[1]Auxiliary materials are available in the HTML. doi:10.1029/2008JB005856.

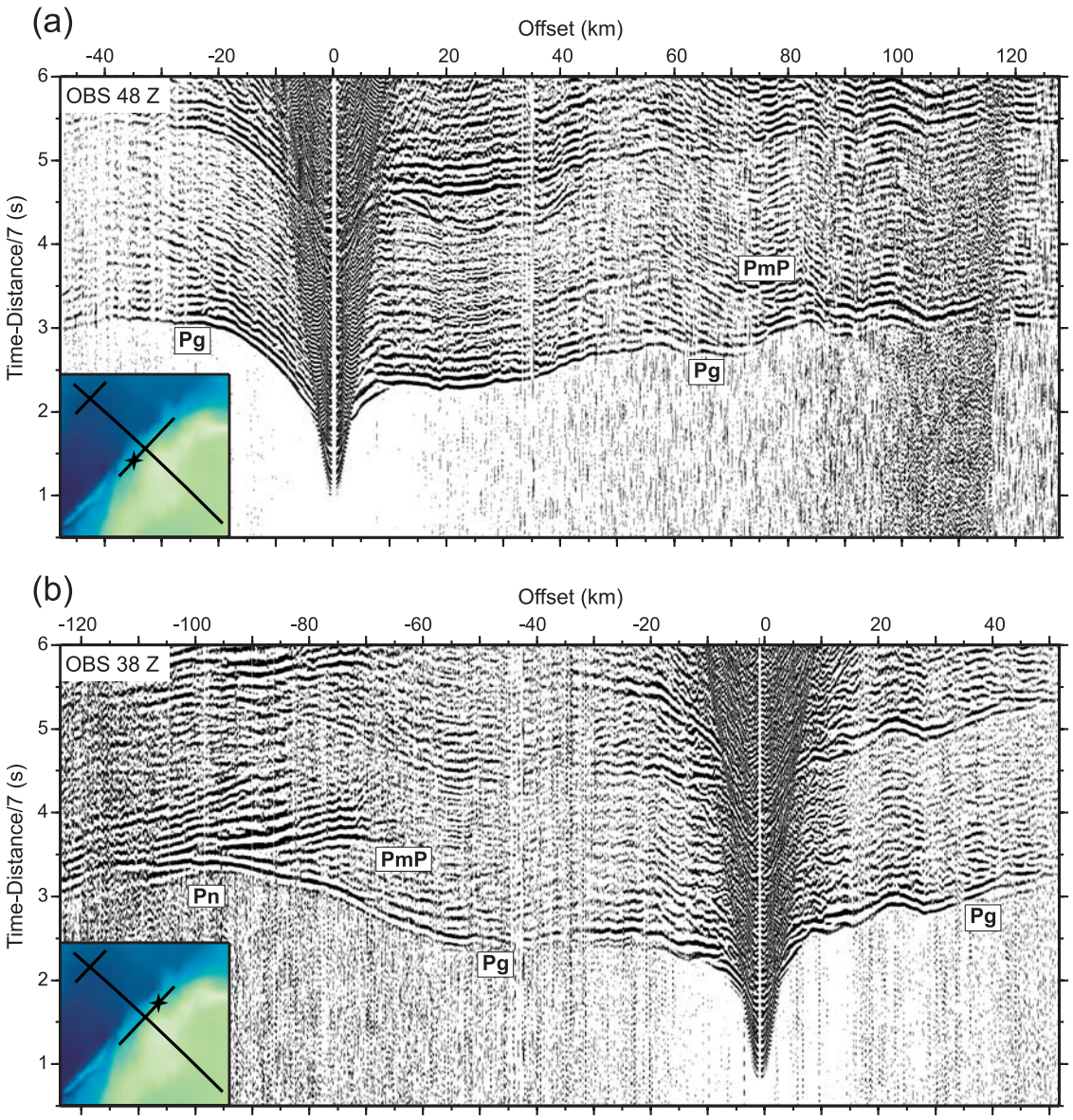

Figure 4. Examples of vertical geophone recordings of wide-angle seismic data from strike line: (a) OBS 48, to the southwest. (b) OBS 38 to the northeast. Traces are scaled to a common maximum amplitude, band-pass-filtered 2–15 Hz, with traveltimes reduced at 7 km/s. Stars on inset show locations of OBS (see also Figure 1).

of shotpoints and OBSs [*Zelt and Smith*, 1992], and arrival picks reassessed where there was a discrepancy of more than 150 ms.

4. Tomographic Traveltime Inversion

[11] We constrained the 2-D crustal velocity model by tomographic inversion of the traveltimes of the main P wave arrivals. This was done in four stages, each one using the results of the previous analysis as input to the next stage in the modeling. Finally, 100 independent tomographic inversions were made with the input models varied randomly across a wide range of geologically realistic depths and velocities with additional errors typical of likely picking errors added to the traveltimes in order to obtain a measure of the spatial variation in uncertainty in the final models. A variety of resolution tests were also constructed. In the following description we use the dip line to explain the procedure.

[12] The first stage was to use the velocimeter and XBT measurements, together with the 10 kHz echo sounder records to constrain the water layer velocity structure and thickness. The sediment layer seismic velocity and thickness was calculated from semblance analysis of the MCS streamer data. In this area the sediments are thin (<1 km), except in the Hatton-Rockall Basin and are well constrained by the streamer data.

[13] The second stage was to use the wide-angle Pg crustal diving wave traveltimes of first arriving phases in a tomographic inversion, using the FAST computer program [*Zelt and Barton*, 1998]. The water and sediment layers were input as a priori constraints and the 2-D velocity model

defined by a uniform 0.1 km by 0.1 km grid. Inversion reduced the χ^2 value of the initial input model from >6 to 3.7, with a final RMS misfit of 109 ms. It was not possible to achieve a better fit without introducing short-wavelength anomalies that were beyond the resolving power of the data set. The final model from this stage is shown in Figure 5a. The upper 5–10 km of the crust is well constrained by crossing raypaths, but the deeper crust is only poorly constrained by some deeper penetrating first arrival diving waves and a small number of Pn mantle refractions (Figure 5b).

[14] Since there are numerous strong wide-angle reflections off the Moho (PmP) with 7850 separate traveltimes on the dip line, these were introduced in a third inversion step using the forward ray-tracing modeling program Rayinvr [*Zelt and Smith*, 1992]. The velocity structure down to 10 km depth constrained by the previous inversion step with FAST was held fixed. Since Rayinvr ray traces through a layered model with interfaces, whereas the previous inversion with FAST used a regular grid of nodes, the Rayinvr model for the top 10 km was constructed by sampling the FAST velocity field over a 1.0 by 0.5 km grid with the rows of the grid forming the layers of the Rayinvr model. The boundaries of the rows were used to represent interfaces, with identical velocities above and below each interface to avoid artificial velocity discontinuities. The lower crust beneath 10 km and extending down to the Moho was represented by a single layer with a uniform vertical velocity gradient, which was allowed to vary laterally.

[15] The final best fit Rayinvr model had an RMS misfit of 120 ms (χ^2 = 1.85), and successfully ray traced 98% of the observed traveltimes (Figures 5c and 5d). We analyzed model uniqueness by testing 10 different starting models with varying initial Moho depths and lower crustal velocities. These show that the lower crust is well constrained over the interval from 50 to 250 km along the model, particularly in the region of primary interest straddling the COT, with little variation from the different inversions in the velocities and Moho depths across this section of the profile. Standard errors from the Rayinvr covariance matrix are typically less than 0.07 km/s for velocity and 0.4 km for Moho depth across this well-constrained region.

[16] Although the Rayinvr model provides a satisfactory fit to the traveltime observations, it has several limitations, chief among which is the user-defined parameterization of the number and node spacing of interfaces, which may lead to bias in the final model. Other limitations include modeling the lower crust as a single layer, which therefore limits resolution of detailed velocity variations within that layer, other than those which can be expressed by a uniform vertical gradient, and the inversion of PmP reflections which permit velocity-depth ambiguity in the Moho which could be resolved if diving waves in the lower crust were inverted simultaneously.

[17] We therefore moved to a final tomographic inversion technique, Tomo2D developed by *Korenaga et al.* [2000], which jointly inverts refraction traveltimes through the model as well as reflection traveltimes from a chosen single reflector, which in our case is the Moho. We used a total of 17,639 Pg arrivals and 7850 PmP arrivals in the dip line inversion. Using a starting model derived from the previous modeling steps, we derive the velocity distribution shown in Figure 5e, which has an overall RMS traveltime misfit of 64 ms (χ^2 = 1.5), comprising an RMS misfit of 62 ms for Pg arrivals and 65 ms from PmP reflections. Compared to the FAST starting velocities there is little change in the velocity structure of the upper crust, which is unsurprising since this part of the model is constrained primarily by diving wave Pg arrivals. However, the lower crustal region has more structure in the Tomo2D inversion than in the previous Rayinvr inversion, which again is consistent with the Tomo2D grid parameterization which allows more detail to be modeled than does the single velocity gradient layer of the Rayinvr inversion.

[18] The Tomo2D model was defined by 59,274 velocity nodes across a 400-km-long by 40-km-deep model domain. The node spacing was 0.5 km in the horizontal direction, with the vertical node spacing increasing from 0.05 km near the surface to 1 km at the base. The Moho reflector was defined by 401 modes with a uniform 1 km spacing. Since we identified only a few unambiguous mantle refraction Pn phases, we did not attempt to invert structure beneath the Moho. Correlation lengths for the inversion are defined in the horizontal and vertical directions as the dimensions of the ellipse about which the inversion samples the model and attempts to fit the observed data [*Korenaga et al.*, 2000], so they represent the minimum size of anomaly which may be resolved. This varies with depth. If the correlation lengths are too small, artifacts at a small scale may be introduced, producing a rough model. We tested a range of different correlation lengths and chose values appropriate to the 9 Hz dominant frequency of the arrivals and the size of the Fresnel zone at the appropriate depth. The final inversions used a horizontal correlation length which increased linearly from 4 km at the seafloor, which is the minimum OBS spacing, to 10 km at the base of the model. The vertical correlation length increased from 0.2 km at the seafloor to 7 km at the base.

[19] We used a 1 km correlation length for the Moho reflector to match the node spacing, which allows the trade-off between velocity and depth to be evaluated properly [*Korenaga et al.*, 2000]. Tests of the velocity-depth trade-off for the Moho reflector were made by repeating the inversions with varying weights applied to the crustal velocity and depth perturbation updates. The depth weighting kernel, w, was varied from w = 0.01 to test the model generated when the inversion favored larger velocity and smaller depth perturbations, through equal weighting with w = 1, to the opposite relative weighting of depth and velocity with w = 100. The fit to all three models is similar (see Figure S1 in the auxiliary material), a consequence of the high number of crossing raypaths in the central part of the model between 50 and 250 km distance, so for the final models we chose equal weighting of velocity and depth updates (w = 1) for the Moho reflector inversions.

4.1. Resolution Tests

[20] Traveltime inversions are inherently nonunique, so we spent considerable effort in assessing the resolution of the model. Since we had a dense data set, a simple test was to split the data into two parts and to invert them separately to investigate the similarity of the two inversions. For this test we chose a simple starting model with a 1-D crustal velocity structure hung beneath the base of the sediments and a flat Moho at 18 km depth (see Figure S2a in the

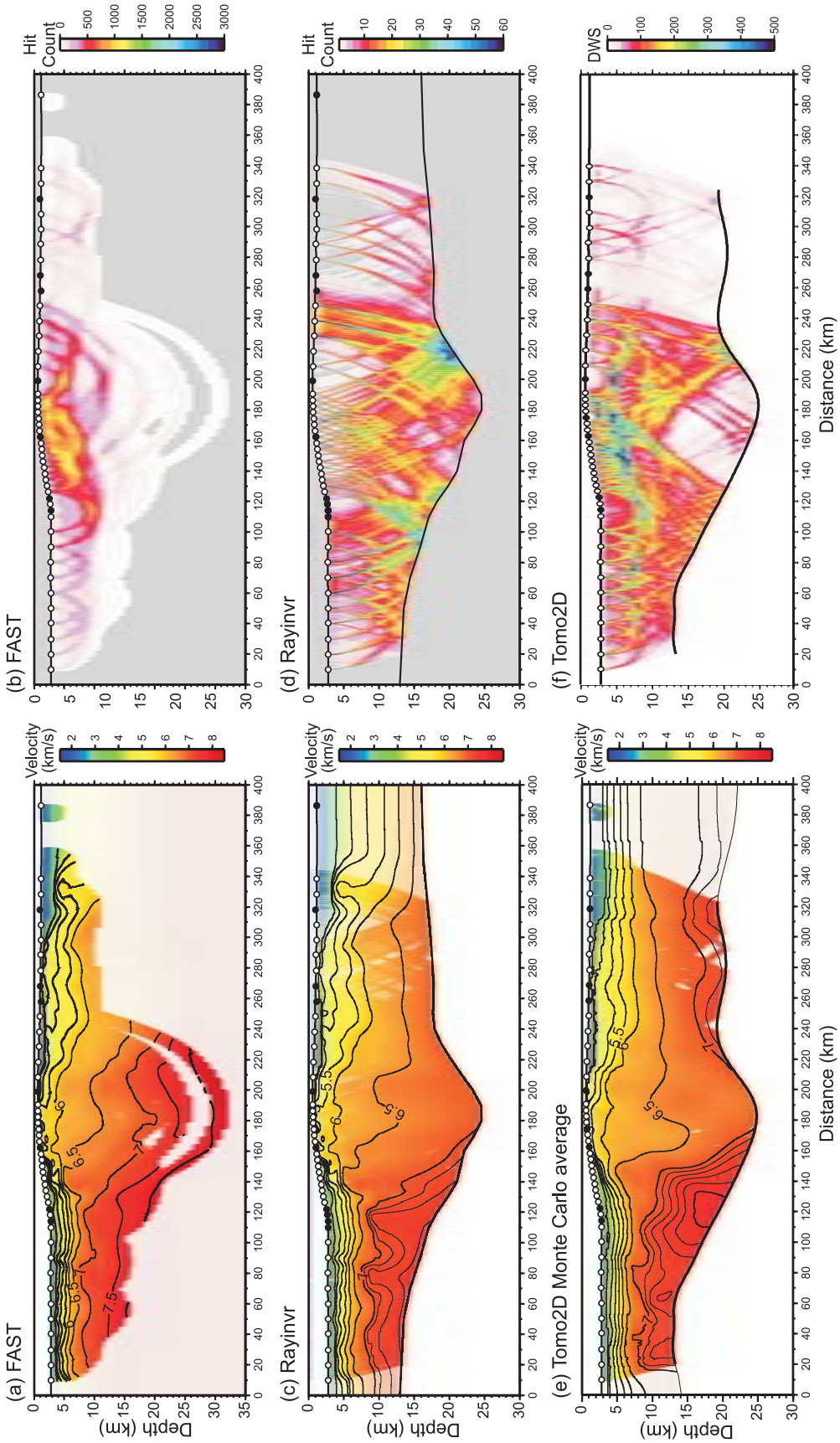

Figure 5. Final tomographic inversion models for the dip line showing the sequence in which successively better inversions were developed: (a) FAST [*Zelt and Barton*, 1998], using only first arrivals from crustal refractions Pg, achieving $\chi^2 = 3.7$ and RMS misfit of 109 ms. (b) FAST ray hit count illustrating ray coverage limited mainly to the upper crust. (c) Rayinvr [*Zelt and Smith*, 1992] forward ray-traced model using the FAST model as a starting point for the upper crust, constrained by both crustal refractions Pg and mantle reflections PmP with $\chi^2 = 1.85$ and RMS misfit of 120 ms. (d) Rayinvr ray hit count showing constraints on different areas of the model. (e) Tomo2D [*Korenaga et al.*, 2000] final model using results from FAST and Rayinvr models in the starting model, with final $\chi^2 = 1.5$ and RMS misfit of 64 ms. (f) Tomo2D derivative weight sum (DWS) showing good constraints on the ray coverage through the crust beneath Hatton Bank, the COT, and the oceanic crust but poorer constraint on the southeastern part of the profile at distances >250 km.

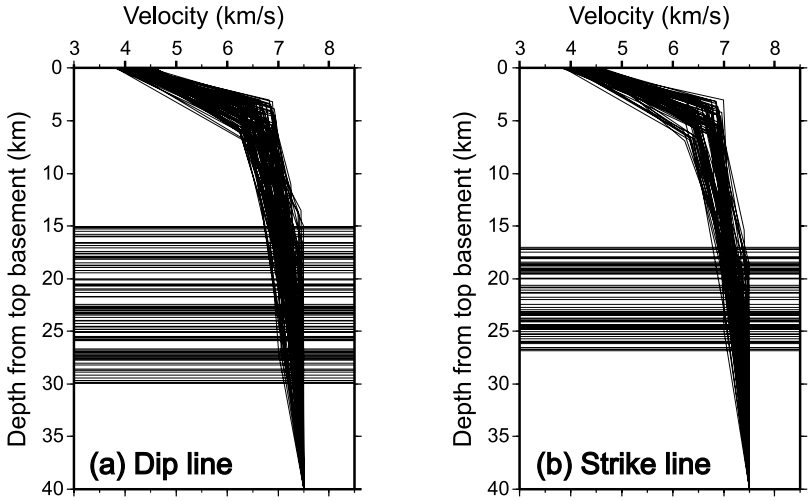

Figure 6. Range of basement 1-D velocity profiles and Moho reflector depths used to generate the starting models for Monte Carlo modeling: (a) dip line and (b) strike line.

auxiliary material). Two independent data sets were made by dividing the OBS into two sets, each distributed along the profile. The long-wavelength structures obtained by inverting the two partial data sets separately are consistent with each other, and with the inversion results using all the OBS along the profile (see Figure S2). Differences are local and small, demonstrating that the major structure is real and is not an inversion artifact.

[21] We also conducted checkerboard tests by introducing alternating regions of positive and negative anomalies onto the final model, and adding random Gaussian noise to the traveltimes. Full details are given in the auxiliary material (Figure S3), but in summary, the locations of the velocity perturbations were recovered well in the inversion, particularly in the upper crust, although the recovered amplitude of the velocity anomalies were only of the order of 1–2% of the background velocity, compared to the input anomalies of 5%. This is normal in checkerboard tests of this type, and is a consequence of the imposed smoothing inherent in the inversion algorithms. For our purposes the most important conclusion is that the significant lateral changes in velocity structure to which we attach geological importance in this paper are all well resolved on an appropriate scale.

[22] In order to assess the robustness of our velocity models and the resolution and uncertainty of the velocities at every position, we used a Monte Carlo technique as an approximation to a Bayesian inference method [*Tarantola*, 1987]. By appropriately randomizing both the starting velocity models and the traveltimes, multiple inversions allow an estimate to be made of the posterior mean and covariance of the solution, from which it is possible to determine the variance of the solution at any point in the model, together with the associated resolution [*Zhang and Toksöz*, 1998; *Korenaga et al.*, 2000]. We use the term ''Monte Carlo ensemble'' to describe the average model which, together with the standard deviation of the velocities and depths illustrates the results from all the individual Monte Carlo inversions. In this study we made 100 Monte Carlo inversions of each profile, using the same inversion parameters as chosen for the best fit model described earlier.

[23] A wide range of starting velocity models was used for the 100 randomized inversions. In each case a 1-D velocity model was hung from beneath the sediments to avoid introducing unnecessary prior information. Since we were not inverting any mantle velocities, a maximum initial velocity of 7.5 km/s was defined at the base of the model. A flat initial Moho reflection depth was input independently of the velocity structure. On the dip line, with its large crustal thickness variations, the starting Moho depth was allowed to vary from 15 to 30 km (Figure 6a), whereas on the strike line with its more restricted variation in crustal thickness, the Moho depth was allowed to vary slightly less between 17 and 27 km depth (Figure 6b), so as to sample well the most likely values.

[24] The observed traveltimes were also randomized before inversion so as to take account of the likely uncertainty in the arrival picks. Simply adding random offsets to each individual pick does not reproduce the likely errors, since it has the effect of producing rough traveltimes with considerable variation between adjacent picks, but an overall average of zero. Following *Zhang and Toksöz* [1998], a more realistic implementation of the likely traveltime errors is to add both a randomized receiver error, which accounts for uncertainties in the clock drift correction and in fine-scale structure beneath the OBS which is below the resolution of the inversion, and a traveltime gradient error which simulates possible user bias in picking along a phase. In the 100 different inversions we applied a random Gaussian noise distribution with $\sigma^2 = 50$ ms for the common receiver uncertainty, and a random Gaussian distribution with $\sigma^2 = 25$ ms/km for the traveltime gradient uncertainty of a picked phase.

[25] The average 2-D velocity structure of all the Monte Carlo inversions for each profile (which we consider to be the best representation of the velocity structure), plus the standard deviation of the average at every point along the profile, is shown in Figures 7 and 8 for the dip and strike lines, respectively. In both cases the final, ensemble average models are strikingly similar to the results of the inversion using the best estimate of the starting model from prior FAST and Rayinvr inversions (e.g., compare Figure 7 with Figure 5e). The model standard deviation calculated from

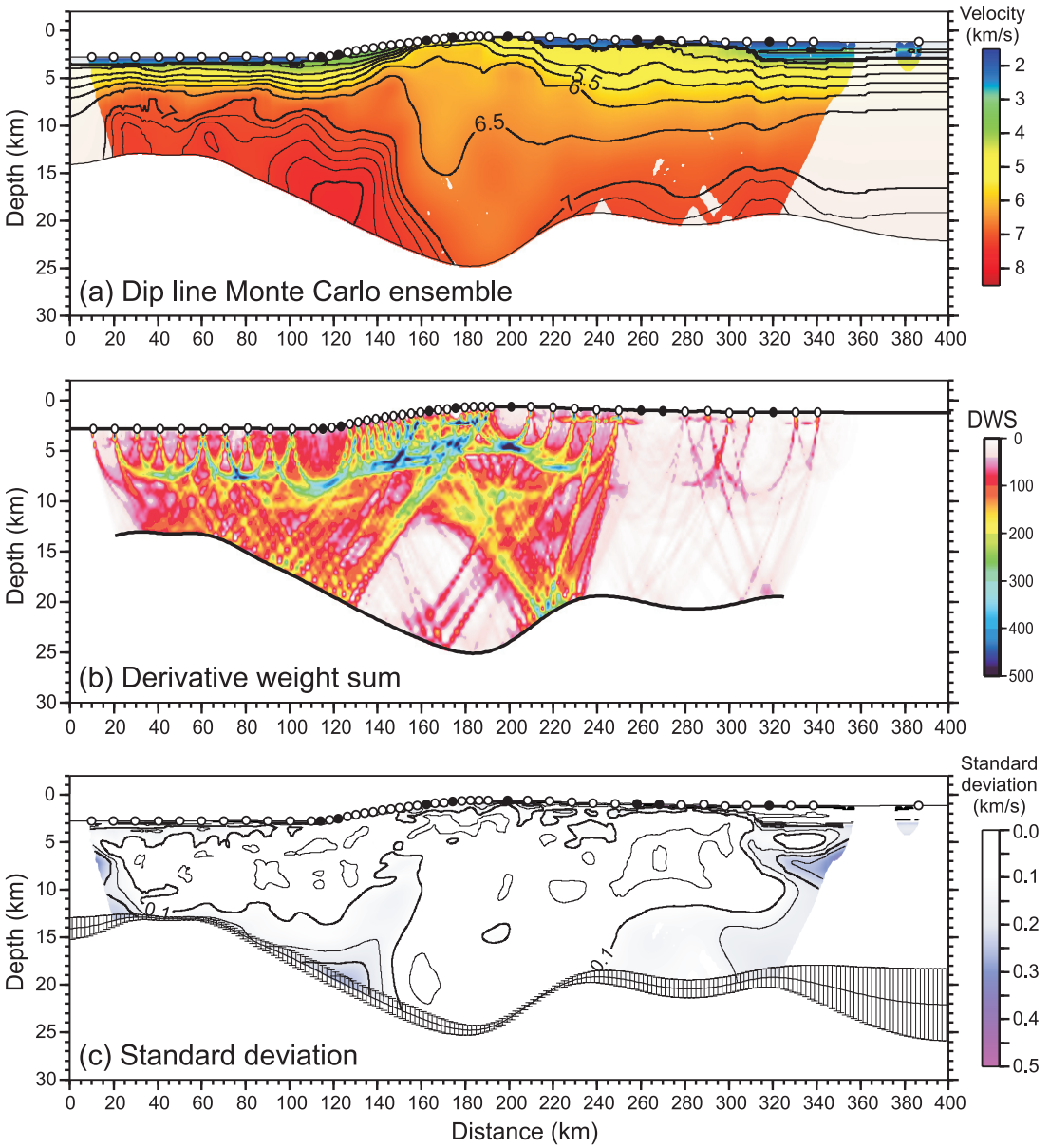

Figure 7. (a) Final dip line Monte Carlo average from 100 randomized starting models, with region of ray coverage highlighted; bold contours every 0.5 km/s; fine contours every 0.1 km/s above 7.0 km/s. (b) Derivative weight sum showing raypath coverage. (c) Model standard deviation with bold velocity contours drawn every 0.1 km/s and fine velocity contours drawn every 0.05 km/s. Error bars on Moho show standard deviation for resolution of depth to Moho.

all 100 Monte Carlo inversions shows that the velocities on both profiles are constrained to better than 0.1 km/s across almost all the model, with the weakest constraint (reaching 0.2 km/s uncertainty) restricted to a small area near the base of the crust at ~130 km on the dip line where the ray coverage is poorest. Unsurprisingly, the velocity constraints are also poorer at the ends of the models. The standard deviation of the Moho reflector depth is mostly in the range 0.6–1.0 km across the central regions of the profiles, consistent with the dominant wavelength at the base of the crust of ~700 m.

[26] In the auxiliary material, we show the observed traveltime picks and calculated traveltimes through the final Monte Carlo ensemble averaged model from all the OBS, together with the raypaths for each calculated traveltime.

4.2. Comparison With Other Velocity Models of Hatton Margin

[27] There are now three independent wide-angle profiles across the Hatton margin, each processed and modeled separately using different methods. So they provide a good opportunity to compare different methods of constraining the crustal structure of a similar part of the margin. In Figure 9 the crustal structures published for each of the three profiles are redrawn at the same scale and then aligned along strike.

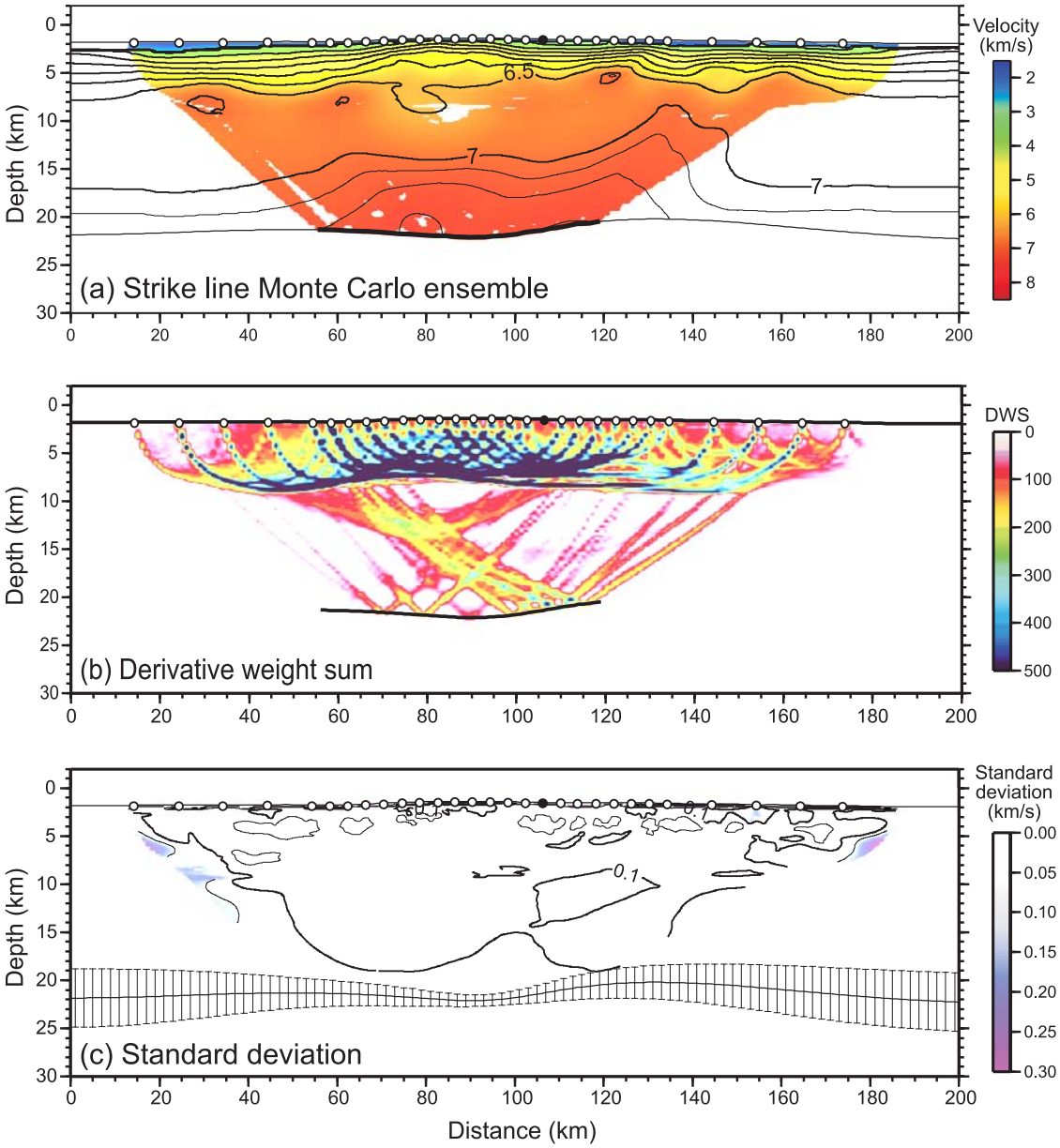

Figure 8. (a) Final strike line Monte Carlo average from 100 randomized starting models, with region of ray coverage highlighted; bold contours every 0.5 km/s; fine contours every 0.1 km/s above 7.0 km/s. (b) Derivative weight sum showing raypath coverage. (c) Model standard deviation with bold velocity contours drawn every 0.1 km/s and fine velocity contours every 0.05 km/s. Error bars on Moho show standard deviation for resolution of depth to Moho.

[28] The first dip section [from *White et al.*, 1987, Figure 9a] was compiled from a series of expanding spread profiles recorded using two ships, one with a multichannel streamer and the other firing either an air gun array or up to 62 explosive shots spaced 1 km apart, ranging in size from 2.1 kg at near offsets to 100 kg at far offsets. The expanding spread profiles were orientated along strike of the margin so as to minimize lateral variations in structure (dotted lines in Figure 1 show locations of profiles). The expanding spread profiles had to be interpreted assuming a one dimensional velocity-depth variation, apart from corrections for the known water and sediment thicknesses beneath each ship. *Cerveny and Psencik*'s [1979] ray-tracing program was used to model the traveltimes, then the velocity structure was refined using amplitudes modeled with *Fuchs and Muller*'s [1971] full reflectivity synthetic seismogram method. The individual one-dimensional velocity profiles from each expanding spread profile at the locations labeled A–H in Figure 9a were then interpolated and contoured to construct the downdip cross section.

[29] The second dip section [see *Morgan et al.*, 1989, Figure 9b] is located along the center points of the expanding spread profiles (labeled HB89 on Figure 1) but was controlled by four OBS (two at each end), and a variable-offset two-ship profile. The energy sources were 105 explosive shots fired every 1.5 km and recorded on both the OBS and the multi-

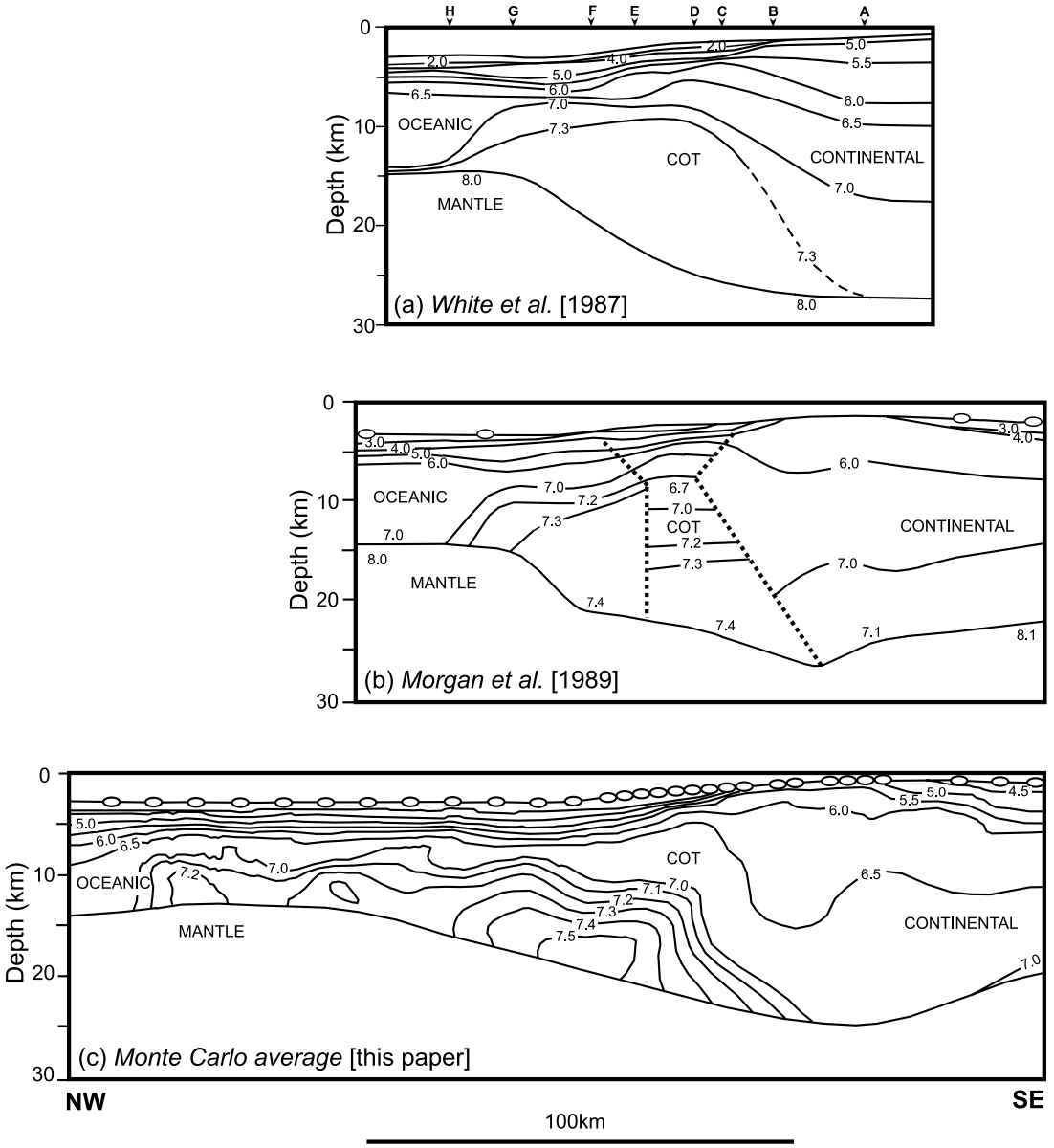

Figure 9. Comparison of models at the same scale of the velocity structure along dip profiles across the Hatton Bank rifted margin, aligned at the same position along strike. COT marks continent-ocean transition. (a) Model from *White et al.* [1987], with details published by *Fowler et al.* [1989] and *Spence et al.* [1989], and constructed by interpolation and contouring between one-dimensional velocity-depth profiles from the midpoints of 8 expanding spread profiles (A–H) orientated along strike at the locations marked along the top of the profile and by dotted lines in Figure 1. The expanding spread profiles used a mixture of explosives and air guns as sources and were modeled using reflectivity synthetic seismograms. (b) Model from *Morgan et al.* [1989] along the dip line marked HB89 in Figure 1 using a downdip two-ship air gun profile with variable offsets plus wide-angle arrivals from four four-component ocean bottom seismometers at locations marked by ellipses at the seafloor, using 105 explosive shots as sources. The data were modeled using Maslov asymptotic ray theory. (c) Final dip line Monte Carlo average velocity structure from this paper modeled using Tomo2D traveltime tomography of arrivals at four-component ocean bottom seismometers marked by ellipses at seafloor.

channel streamer. The traveltime data were modeled using Maslov asymptotic ray theory [*Chapman and Drummond*, 1982], which allows for two-dimensional structure. The starting model for the crustal velocity model was derived from the expanding spread profiles. Discontinuities were introduced in the region of the COT where the velocities of the lower crust were higher than normal, introducing a small low-velocity zone between the extrusive lavas that produce seaward dipping reflectors on the COT and the underlying lower crust.

[30] The third dip section (Figure 9c from the Monte Carlo average of the randomized Tomo2D inversions reported in

this paper) is about 30 km along strike to the south of the previous two profiles (Figure 1). It was recorded using a large air gun source array and a dense array of four-component OBS as described in section 2.

[31] Despite the different methodologies of both recording and interpreting the wide-angle data, the main features of all three different profiles are consistent. They each show a relatively narrow transition from continental to oceanic crust, and each one requires high-velocity material in the lower crust of the COT. The actual crustal velocities inferred are similar in all three profiles (generally within 0.1 km/s). The overall crustal thickness and its variation across the continental margin are also similar. It is certainly encouraging to have this degree of agreement in the main features that are used for interpretation. However, the more interesting question lies in the differences between the profiles. These differences lie mainly in the resolution that the different methods provide, and in the constraints that can be placed on the uncertainties in the models.

[32] Not surprisingly, the resolution increases from the smoothest model in Figure 9a, interpolated from one-dimensional velocity-depth profiles, through the variable-offset model in Figure 9b to the model constrained by closely spaced OBS in Figure 9c. Perhaps more importantly, the denser wide-angle coverage provided by the multiple crossing raypaths from the closely spaced OBS array in the most recent profile allows an automated tomographic inversion to be employed. This is better than the trial and error forward ray tracing modeling used to construct Figure 9b because although that model fits the arrival times within their estimated uncertainties, the sharp interfaces marked by the dotted lines have been inserted by the modeler. Although at first sight they may appear to indicate high-resolution control on the discontinuities, in practice they are only one possibility from an infinite number. Indeed, geologically, it is unlikely that such sharp subvertical discontinuities exist in highly stretched and heavily intruded crust. In contrast, the average structure from 100 inversions with randomized starting models shown in Figure 9c shows a better depiction of the structure that can be constrained unambiguously by the data. It is theoretically possible that the true structure contains sharp subvertical discontinuities within it, but that the multiple inversions mask that solution – if so, that is a helpful result, because it means that the data do not *require* a sharp discontinuity, so we could not put prominence on one in our interpretation. However, a corollary to this statement is that sometimes the profile does indeed contain sharp discontinuities that we do know about, such as the seafloor interface and the sediment-basement interface. If we did not force the inversion to introduce these interfaces, then it would produce smoothed velocity changes across them, with the smoothness controlled mainly by the grid size of the inversion. In the inversion modeling it is normal to introduce a sharp discontinuity at the seafloor and to heavily damp the structure, such as sediment thickness that is known independently (for example from seismic reflection profiles).

[33] Perhaps more significantly, the newer and denser data sets enable an objective measure of the uncertainty in the velocities and depths to be placed on the inversion models as well as using them to define a ''best'' average model. The combination of ray densities as measured by the derivative weight sum and the standard deviation of all 100 inversions from randomized starting models (as shown in Figures 7b, 7c, 8b, and 8c) give a good indication both of the areas of the model that are constrained well by the data, and of how much deviation in velocity structure is allowable in any particular area of the model. By contrast it is difficult to gain any constraint on the possible range of velocity models from the interpolated 1-D models of Figure 9a. In the case of the forward ray-traced model which produced Figure 9b, *Morgan et al.* [1989] gave no indication of the allowable range of models but commented that it was hard to find a model which matched all the data. They report trying 700 different models before finding a satisfactory fit. In such circumstances, the ray coverage is perhaps the best indication of which parts of the model are constrained, while checkerboard tests provide an indication of the magnitude and dimensions of velocity perturbations that could in principle be resolved.

[34] It is worth commenting that the models shown in Figures 9a–9c have been derived primarily from the traveltimes of P waves. Clearly there is much more information available in the seismic data than just the traveltimes. Where converted S waves are generated, then they can provide constraints on the Poisson's ratio of the rocks, which may help with interpretation [e.g., *Eccles et al.*, 2007]. The obvious next step is to use the amplitudes of the arrivals to refine the velocity structure. Amplitudes are particularly sensitive to the sharpness of velocity changes and to velocity gradients. Hitherto it has proven possible to use amplitude information with the assumption of local 1-D structure, as *Fowler et al.* [1989] demonstrated in deriving the structure shown in Figure 9a. As computer processing power has increased, it has become realistic to derive acoustic waveform inversion constraints provided the models are limited in size and contain good low-frequency content to constrain the longer-wavelength structure [e.g., *Brenders and Pratt*, 2007]. At present, the computing power that would be required means that it is not realistic to make full elastic inversions of whole crustal models similar to those shown here from the Hatton margin, but doubtless it will be in due course. The expectation is that the long-wavelength structure shown in Figures 7–9 would not change, but the constraints on local discontinuities and velocity gradients would improve, giving better resolution.

5. Interpretation

[35] In the following sections we discuss in turn the main tectonic provinces crossed by the dip line profile. At the continentward (southeastern) end the profile crosses the Mesozoic Hatton Basin followed toward the northwest by the Hatton Bank continental block, then the COT with its characteristic seaward dipping reflectors in the upper crust and finally oceanic crust with seafloor spreading magnetic anomalies.

5.1. Hatton Basin

[36] The Hatton Basin is the least constrained portion of the profile, due to the sparse OBS spacing. Nevertheless, good wide-angle Moho reflections were recorded, constraining the crustal thickness as 19–21 km, with a Moho depth uncertainty of ~1 km. The basin was formed by Mesozoic stretching before the Tertiary continental breakup. Our dip profile (Figure 2) crosses the flank of the late Paleocene

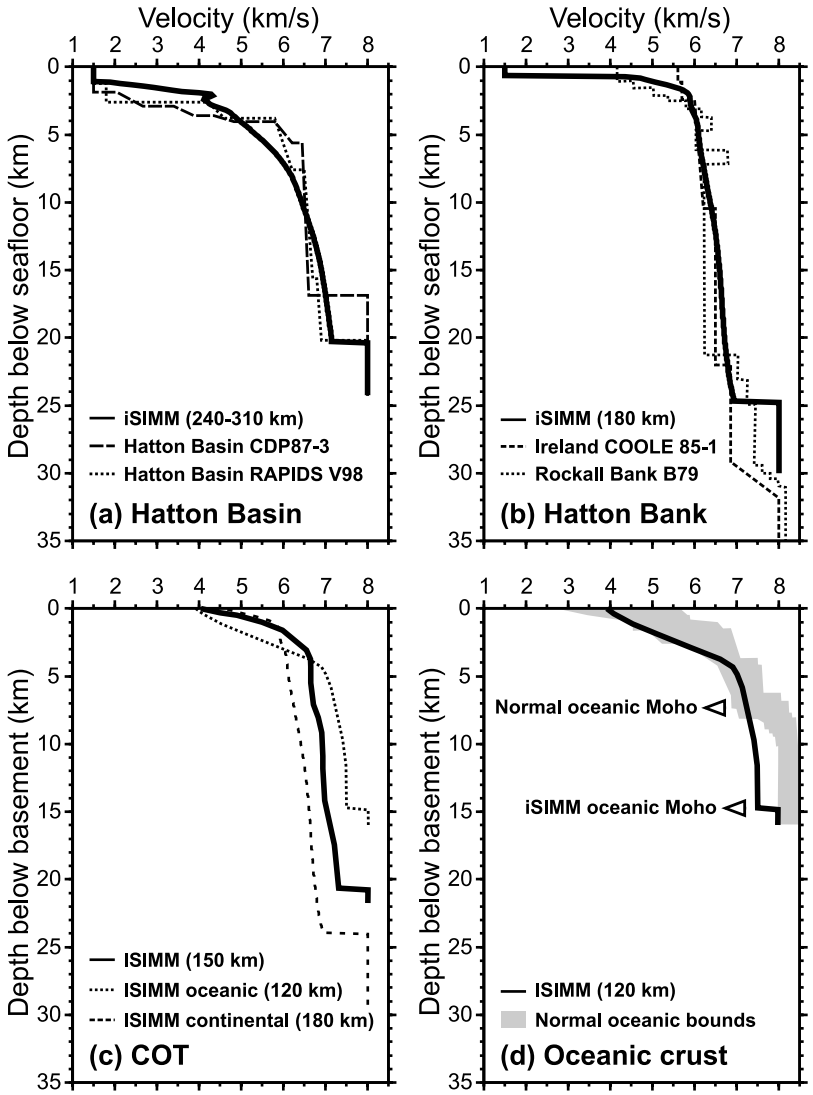

Figure 10. (a) Comparison of the average crustal velocity structure in Hatton Basin (averaged from 240 to 310 km along iSIMM dip profile) with the structure beneath Hatton Basin ~55 km to the SW (CDP87-3 [*Keser Neish*, 1993]) and 200 km to the SW (RAPIDS V98 [*Vogt et al.*, 1998]). (b) Comparison of Hatton Bank velocity structure at 180 km along dip profile with the structure beneath Rockall Bank (B79 [*Bunch*, 1979]) and Ireland (COOLE 85-1 [*Landes et al.*, 2005]). (c) Velocity structure of the continent-ocean transition at 150 km along dip profile, with comparison curves from continental crust at 180 km and oceanic crust at 120 km along profile. (d) Velocity structure of oceanic crust at 120 km along dip profile compared to normal oceanic crust (gray shading, all Atlantic oceanic profiles away from fracture zones and plumes from *White et al.* [1992]). The iSIMM velocity profiles are constrained to the base of the crust only, so an appropriate velocity contrast has been added to indicate the position of the Moho. Note that curves in Figures 10a and 10b show depth below sea level, while curves in Figures 10c and 10d show depth below the top of the basement.

Lyonesse igneous complex, with extrusive lavas covered by a thin veneer of Cenozoic sediments [*Hitchen*, 2004]. The Hatton Basin was submarine at the time of continental breakup, with the western paleoshoreline marked by a steep basalt escarpment (at 310 km on Figure 2). Eocene fan deltas formed at the base of this scarp [*McInroy et al.*, 2006], and the Hatton Basin was filled subsequently by ~2 km of Cenozoic sediment.

[37] The crustal thicknesses we deduce for the Hatton Basin are similar to those reported from profile CDP87-3 some 55 km to the southwest by *Keser Neish* [1993] and from the RAPIDS profile about 200 km away by *Vogt et al.* [1998] (see Figure 10a). If we assume that the crystalline basement thickness before stretching was 28 km, as suggested by the nearest wide-angle seismic profiles on Rockall Bank [*Bunch*, 1979] and in Ireland [*Landes et al.*, 2005], then we infer a Mesozoic stretching factor of 2.2 ± 0.3 in Hatton Basin (Table 1). This is considerably less than the probably contemporaneous stretching in nearby Rockall Trough to the east [*Joppen and White*, 1990].

Table 1. Stretching Factors Across Rockall Plateau[a]

	Source	Depth to Moho (km)	Crustal Thickness (km)	Stretching Factor
Ireland	*Landes et al.* [2005]	29.8–31.8 ± 1	28 ± 1	1.0
Rockall Bank	*Bunch* [1979]	29.8–31.0 ± 1	28 ± 1	1.0
Hatton Basin	iSIMM, this paper	20.4 ± 0.90	12.5 ± 1.1	2.24 ± 0.3
Hatton Bank	iSIMM, this paper	24.8 ± 0.55	22.5 ± 0.75	1.24 ± 0.1

[a]The thickness under Ireland and Rockall Bank is used as prestretching reference thickness. The Moho beneath both Ireland and Rockall was interpreted as a transition zone. Uncertainties in the depth to Moho and crustal thickness for both Ireland and Rockall were estimated to be ±1 km. Uncertainties in crustal thickness along the iSIMM line take into account both the error in depth to Moho and error in identifying the top of the crystalline basement.

5.2. Hatton Bank

[38] Hatton Bank is a block of continental crust with a maximum thickness of 23 km between the Hatton Basin on the east and the COT on the west. It has a thin veneer of Cenozoic sediments, only 50 m thick in the shallowest portion. The Cenozoic sediments are underlain by a 1.2 km thick layer with a steep velocity gradient from 4.7 km/s at the top to 5.5–5.9 km/s at the base (Figure 10b). Seismic profiles and shallow drilling in the area shows that Hatton Bank is covered by a layer of extruded basalts, but that in places they have been eroded to expose underlying Mesozoic and possibly Paleozoic sediments [*Hitchen*, 2004].

[39] The bulk of the crust beneath the thin sedimentary and basalt section comprises material with a low velocity gradient from 5.5 to 5.9 km/s at the top to 6.94 ± 0.06 km/s at the base (Figure 10b). This is typical of the crystalline crust found beneath the adjacent Rockall Bank continental fragment [*Bunch*, 1979] and the closest continental mainland beneath Ireland [*Lowe and Jacob*, 1989; *Landes et al.*, 2005], although it is here some 5 km thinner than beneath the mainland. From this we deduce that Hatton Bank has been stretched by a factor of 1.2 ± 0.1 (Table 1).

5.3. Continent-Ocean Transition

[40] The transition from the continental crust of Hatton Bank to the oldest fully oceanic crust with well-developed seafloor spreading magnetic anomalies is extremely narrow, only some 40 km wide (between 130 and 170 km along the dip profile, Figure 7a). Velocities in the lower crust of the COT are intermediate between those of the adjacent continental Hatton Bank on the east and the oceanic crust on the west (Figure 10c). *White et al.* [2008] showed that a similarly narrow COT has been found north of the Faroes and that the velocity cross section of both the Faroes and Hatton COTs are remarkably similar. However, this is in marked contrast to the reported 150-km-wide zone of transitional crust on the conjugate Greenland margin [*Korenaga et al.*, 2000, 2002; *Hopper et al.*, 2003]. We shall return later to the asymmetry of the conjugate margin and possible reasons for it.

5.4. Oceanic Crust

[41] The oldest oceanic crust immediately adjacent to the COT is identified by seafloor spreading magnetic anomaly 24 at the foot of the continental slope near the termination of the arcuate SDRs. It exhibits a classic oceanic crustal structure, an uppermost layer 2 with a high-velocity gradient underlain by a lower velocity gradient layer 3 down to the Moho. The transition between layers 2 and 3 occurs at a velocity of about 6.7 km/s (Figure 10d).

[42] The seismic profile modeled here spans 120 km of oceanic crust along the dip profile, which covers the first 8 Ma of seafloor spreading following breakup at ~54 Ma. There is a consistent pattern as the crust becomes younger of a decreasing thickness and a concomitant decrease in the average velocity of the lower crust, with the highest velocity found in the oldest and thickest oceanic crust adjacent to the COT. A similar result has been reported by *Parkin and White* [2008], who independently modeled just the oceanic section of this profile, and extended it out to younger oceanic crust generated at 39 Ma. The oceanic crust is everywhere thicker than the normal segment-averaged crustal thickness of 6.4 ± 0.8 km [*White et al.*, 1992; *Bown and White*, 1994]. Weak gravity lineations at ~48 Ma and ~39 Ma visible on both sides of the ocean basin may be caused by small crustal thickness increases similar to those that produce the V-shaped ridges on the young crust of this ocean basin [*Parkin and White*, 2008], but they are beyond the extent of the profile we report here.

5.5. Continent-Ocean Transition: Upper Crust and Extrusive Basalts

[43] The extrusive basalts on the COT form a series of seaward dipping reflectors (SDRs). On dip profiles they often exhibit a characteristic convex upward shape, as a result of crustal stretching and subsidence contemporaneous with their emplacement [*Mutter et al.*, 1982]. Although their present dip is seaward, the lava was emplaced by landward directed flow from a subaerial rift. The basalt sequence reaches at least 5 km at its thickest on the COT and thins to ~1.5 km over the shallowest part of Hatton Bank. Similar SDR sequences are found along all the North Atlantic volcanic margins [e.g., *Larsen and Jakobsdottir*, 1988; *Barton and White*, 1997b; *Holbrook et al.*, 2001].

[44] In Figure 11 we show a compilation of interpretations of the upper crustal structure that shows the SDR morphology from a grid of MCS profiles around the iSIMM lines reported here. Figures 11b and 11c are from strike profiles and Figures 11d–11h from dip profiles: Figures 11b, 11d, and 11e are redrawn at the same scale from sources listed in Figure 11 caption, while the others are new interpretations either from the iSIMM cruise reported here or from the 1985 Hatton Bank cruise [*White et al.*, 1987]. Comparison with our wide-angle velocity tomography shows that below a carapace of thin Cenozoic sediments the seismic velocity of the layered basalts exhibit a high velocity gradient, with velocities increasing from 3.5 km/s at the top of the sequence to 5.5–6.5 km/s at the base. We interpret the velocity gradient through the basalts as caused mainly by the increase in pressure with depth and the concomitant closure in fractures and pore space and in

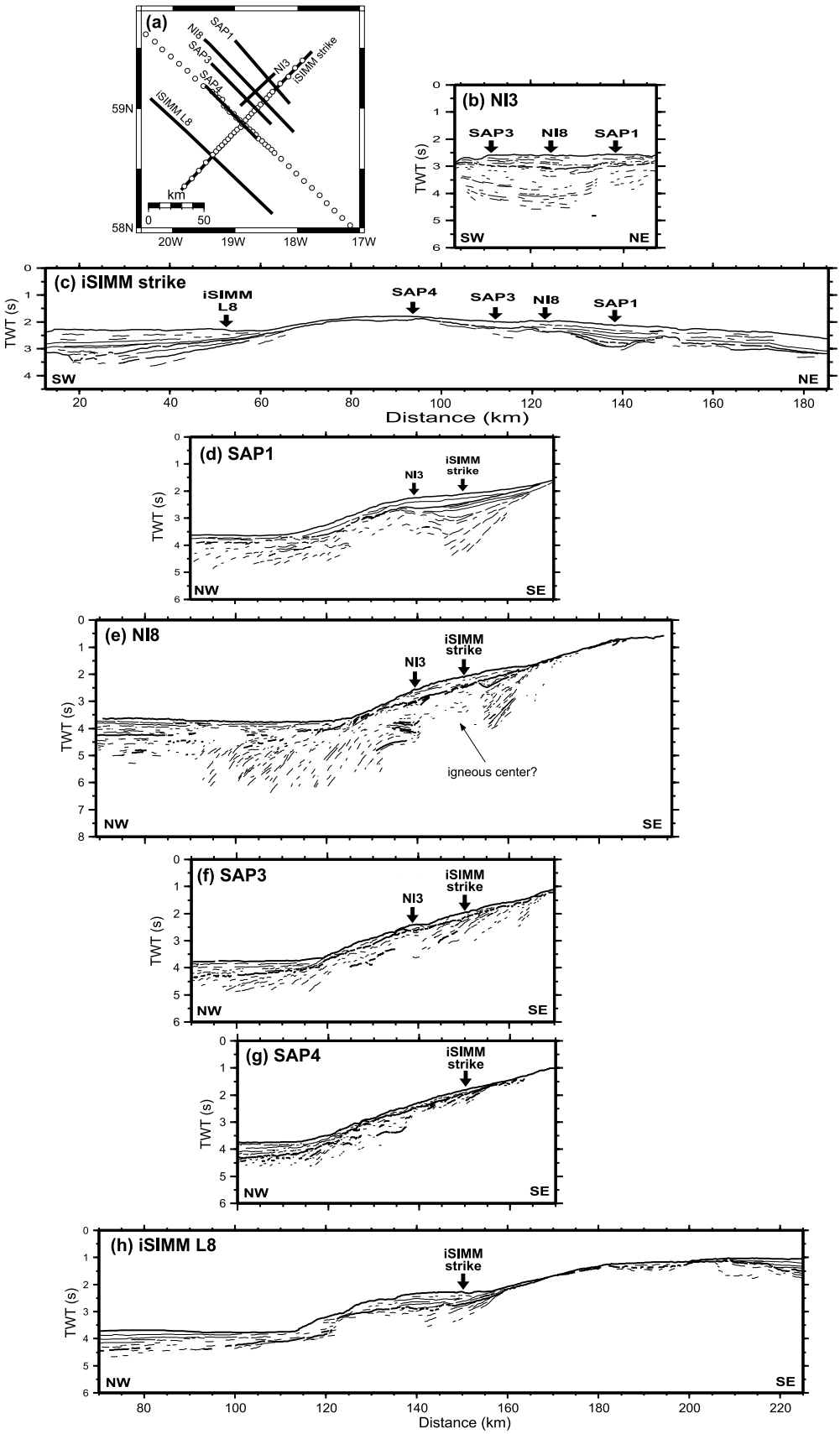
(a)
NI8
SAP1
SAP3
SAP4
NI3
iSIMM strike
iSIMM L8
59N
58N
km
0
50
20W
19W
18W
17W
(b) NI3
SAP3
NI8
SAP1
TWT (s)
SW
NE
(c) iSIMM strike
iSIMM L8
SAP4
SAP3
NI8
SAP1
TWT (s)
SW
NE
Distance (km)
(d) SAP1
NI3
iSIMM strike
TWT (s)
NW
SE
(e) NI8
NI3
iSIMM strike
igneous center?
TWT (s)
NW
SE
(f) SAP3
NI3
iSIMM strike
TWT (s)
NW
SE
(g) SAP4
iSIMM strike
TWT (s)
NW
SE
(h) iSIMM L8
iSIMM strike
TWT (s)
NW
SE
Distance (km)

Figure 11

part from filling of pore space by secondary minerals and a reduction in alteration with depth.

[45] There are two main packages of SDRs on most of the Hatton continental margin, imaged best on profile NI8 (Figure 11e), but also evident on the other dip lines. The upper set of SDRs are thinner and more planar than the lower set which span the COT. The planar geometry of the upper set suggests that they were emplaced onto continental crust with greater flexural strength and less extension than those on the highly extended and intruded COT, which exhibit pronounced convex-up curvature. The two packages are separated on profile NI8 (Figure 11e) by a seismically opaque region extending from 140 to 155 km which could be either a continental fault block or an igneous intrusion. On the Edoras Bank margin to the south, a similar geometry was interpreted as a fault block, with lavas ponding against it on the landward side [*Barton and White*, 1997a, 1987b]. However, the limited lateral extent, high density and magnetization of the feature on the Hatton margin led *White et al.* [1987], *Spence et al.* [1989], and *Morgan et al.* [1989] to interpret it as an igneous center.

[46] On strike lines the SDRs are imaged as subhorizontal reflectors (Figures 11b and 11c), consistent with the basalts having been extruded from fissure swarms aligned parallel to the rift. The thickness of the reflective basalts varies along strike, as they flowed to fill lows in the topography.

[47] Immediately beneath the basalt sequence on the COT, the crustal velocity is >6.5 km/s. This is higher than the velocity at the same depth beneath the continental block of Hatton Bank, although we expect the rocks to be the same. The reason is probably that on the COT there are sills and feeder dykes intruded into the consolidated sediments that form the upper part of the prebreakup continental crust, and these raise the crustal seismic velocity. A similar effect, also attributed to igneous intrusions has been reported from the Ethiopian rift, where there is an abrupt increase from typical continental crustal velocities to crust with P wave velocities that are 5–10% higher (>6.5 km/s) in the region of the Boset volcanic rift [*Mackenzie et al.*, 2005].

[48] A striking characteristic of the upper crust of the COT, in addition to its narrowness, is the absence of crustal fault blocks such as are typically found on nonvolcanic margins, and indeed are inferred to be present on the conjugate east Greenland margin based on ODP drilling and high-resolution seismic profiles [*Larsen and Saunders*, 1998]. It is likely that initial fault blocks were obliterated by continued heavy igneous activity in the narrow band of the COT, or that the intrusion of melts at ~1300°C, well above the melting point of the shallow continental crust, created ductile conditions that allowed large amounts of crustal extension without brittle faulting.

5.6. Continent-Ocean Transition: Lower Crust

[49] The crustal thickness decreases rapidly across the COT, from 23 km to 18 km over the 40 km interval from 170 to 130 km distance (Figure 12). The lower crust over this same interval exhibits high seismic velocities, intermediate between the velocities of the continental Hatton Bank crust on the landward side and the higher velocities of the oceanic crust of the Iceland Basin on the seaward side (Figures 10c). The high velocities are indicative of the presence of igneous rocks in the lower crust, and are much higher than found in the continental crust of NW Europe that is not affected by Tertiary igneous activity [*White et al.*, 1987]. There is some indication that the high-velocity rocks extend a short distance landward beneath Hatton Bank at the very base of the crust (Figure 7a), but such lateral intrusion is apparently limited, with the majority remaining beneath the region of igneous extrusion marked by the seaward dipping reflectors on the COT.

[50] Although our MCS profiles on the Hatton margin do not image the lower crust, on another iSIMM profile north of the Faroe Islands, a deep penetration MCS profile shows that a similar narrow zone of elevated (>7.0 km/s) velocities in the lower crust of the COT is coincident with extensive lower crustal reflections interpreted as sills [*White et al.*, 2008]. Using the insights from the Faroes profile reported by *White et al.* [2008], we therefore interpret the lower crustal velocities on the Hatton profile as representing a mixture of igneous intrusives produced during continental breakup and the residual continental crust on the COT into which they are intruded.

[51] In Figure 12 we show the way in which the average velocity of the lower crust increases across the COT along the Hatton dip profile. It shows an increase of 0.59 ± 0.17 km/s from continental to oceanic crust with the maximum velocity being reached as the first (oldest) oceanic crust of the Iceland Basin is formed. There is excellent agreement of the velocity of the lower crust between the dip and strike profiles at the intersection point, although they were modeled independently.

5.7. Melt Generation

[52] A key question is what causes the generation of huge quantities of igneous rock on volcanic rifted continental margins such as this one. The suggestion that the main mechanism was decompression melting as hotter than normal mantle rose beneath a lithospheric rift was first made by *White et al.* [1987] to explain the seismic high-velocity lower crust mapped from seismic data from this same Hatton continental margin; a similar suggestion to explain melting during stretching of the nonvolcanic Biscay

Figure 11. Line drawings of unmigrated time sections from MCS reflection profiles recorded by the 1985 Hatton and the 2002 iSIMM surveys across the Hatton margin. (a) Location map, with circles showing positions of OBS on iSIMM profiles. (b) Strike line NI3 from *White et al.* [1987] using same distance scale as Figure 11c. (c) Strike line from iSIMM survey reported here. (d) Dip line SAP1 from *White et al.* [1987]. (e) Dip line NI8 from *Spence et al.* [1989] showing crossing of igneous center discussed in text. (f and g) Dip lines newly interpreted from original profiles. (h) Dip line iSIMM L8 processed by N. Hurst (personal communication, 2007) and newly interpreted. Dip lines are all aligned on intersection with iSIMM strike profile at 150 km distance along dip line scale.

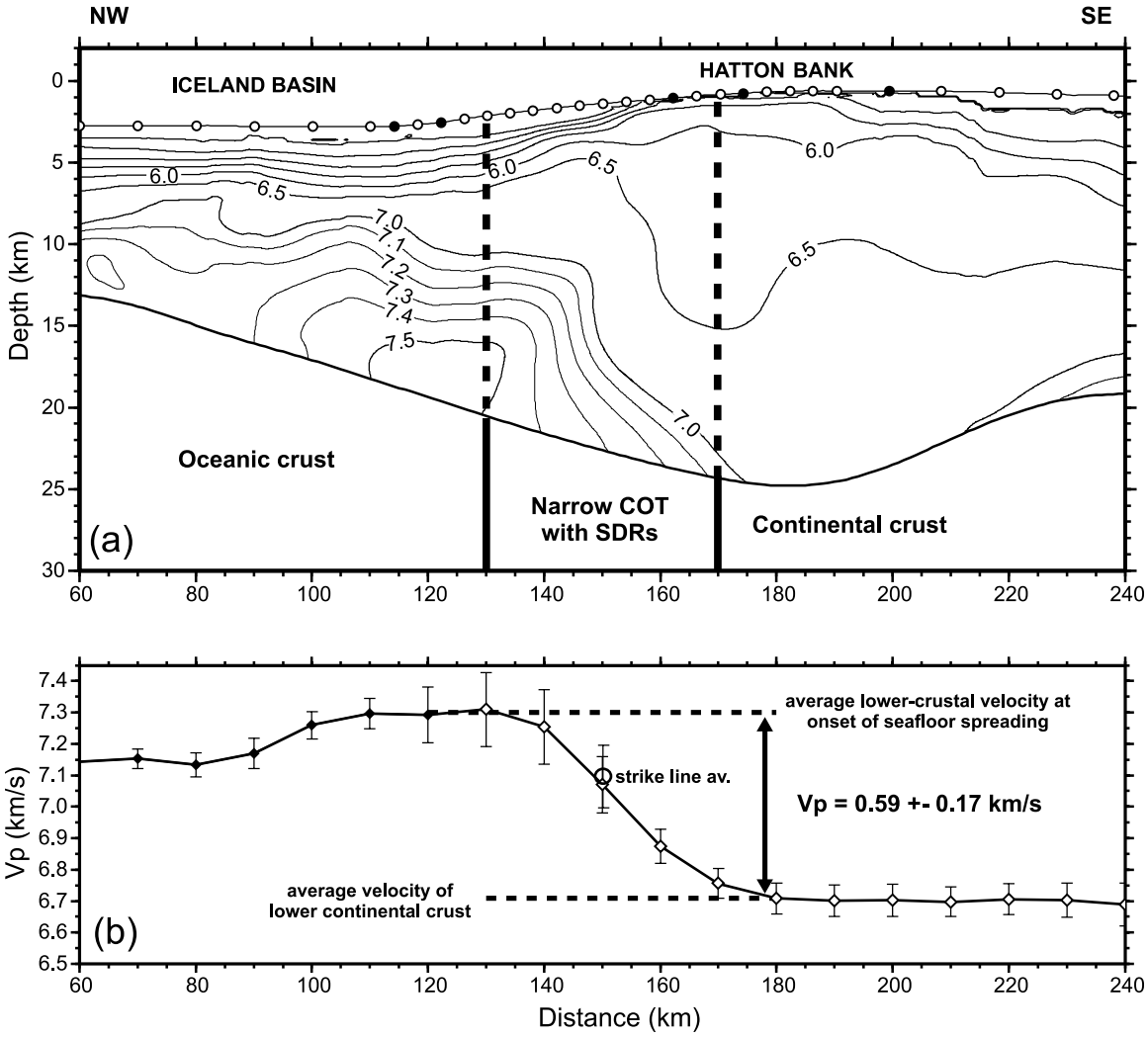

Figure 12. (a) Velocity structure from average of Monte Carlo tomographic inversions along dip line (from Figure 8), with main interpretation of crustal types superimposed. (b) Mean lower crustal velocities along the dip profile calculated across horizontal windows of 10 km. Open diamonds are calculated for an 11 km thick section above the Moho, with large open circle the average for the intersecting strike profile between 70 and 110 km along the strike line. Black diamonds indicate lower crustal velocities from oceanic crust calculated for the crust with velocities > 6.7 km/s (which represents layer 3 section least affected by the changes in porosity and alteration that exert a strong control on the shallower, layer 2 velocities).

continental margin above mantle of normal temperature had been made earlier by *Foucher et al.* [1982]. Several recent models have suggested that a mantle thermal anomaly is required to explain the excess magmatism on volcanic margins, sometimes also with small-scale convection [e.g., *Nielsen and Hopper*, 2002, 2004]. More recently, alternative suggestions to explain the melting on volcanic margins have included small-scale convection under the rift without a significant temperature anomaly in the mantle, or the presence of fertile mantle beneath the rift which therefore was more readily melted [e.g., *Mutter and Zehnder*, 1988; *Korenaga et al.*, 2000, 2002]. We note, however, that the fertile mantle source normally invoked is an iron rich layer, but *Nielsen and Hopper* [2004] showed that the high density of such a layer would prevent it from convecting. *Nielsen and Hopper* [2004] also investigated the possibility of a water rich layer allowing additional melting because the wet solidus is at a much lower temperature than the dry solidus, but again they could not get a large volume of melt produced in their models because little melt was produced before the mantle dehydrated and returned to the dry solidus and a much higher viscosity.

[53] We will not repeat here a discussion of the broader evidence that may be used to test the mantle plume theory for melt generation on volcanic rifted margins, since that has been reviewed recently by *Campbell* [2007] and by others in numerous articles on different volcanic margins. Instead we use the new constraints on the seismic velocity and thickness of the igneous crust on the margin to address the narrower question of whether it can be explained adequately by the presence of a thermal anomaly in the mantle during rifting, or whether either the occurrence of

active convection or the presence of fertile mantle must be postulated.

[54] A powerful tool to address this question is a plot of total igneous thickness, h versus the seismic velocity, v_p of the primary melt, as introduced by *Korenaga et al.* [2000] and *Holbrook et al.* [2001]. In Figure 13a we show a summary from *White et al.* [2008] of the main influences on an h-v_p plot of different possible processes. Because both h and v_p increase monotonically and to first order linearly with the temperature of the parent mantle, it is possible to discriminate between an increase in igneous thickness caused by a mantle temperature increase (which causes both h and v_p to increase, as shown by diagonal shaded arrow on Figure 13a), from mantle convection at a constant temperature under the rift (which causes h to increase but v_p to remain almost the same, as shown by the horizontal arrow on Figure 13a), or increased mantle fertility (which may cause v_p to decrease as h increases, diagonal dashed arrow in Figure 13a). However, it is important to be aware

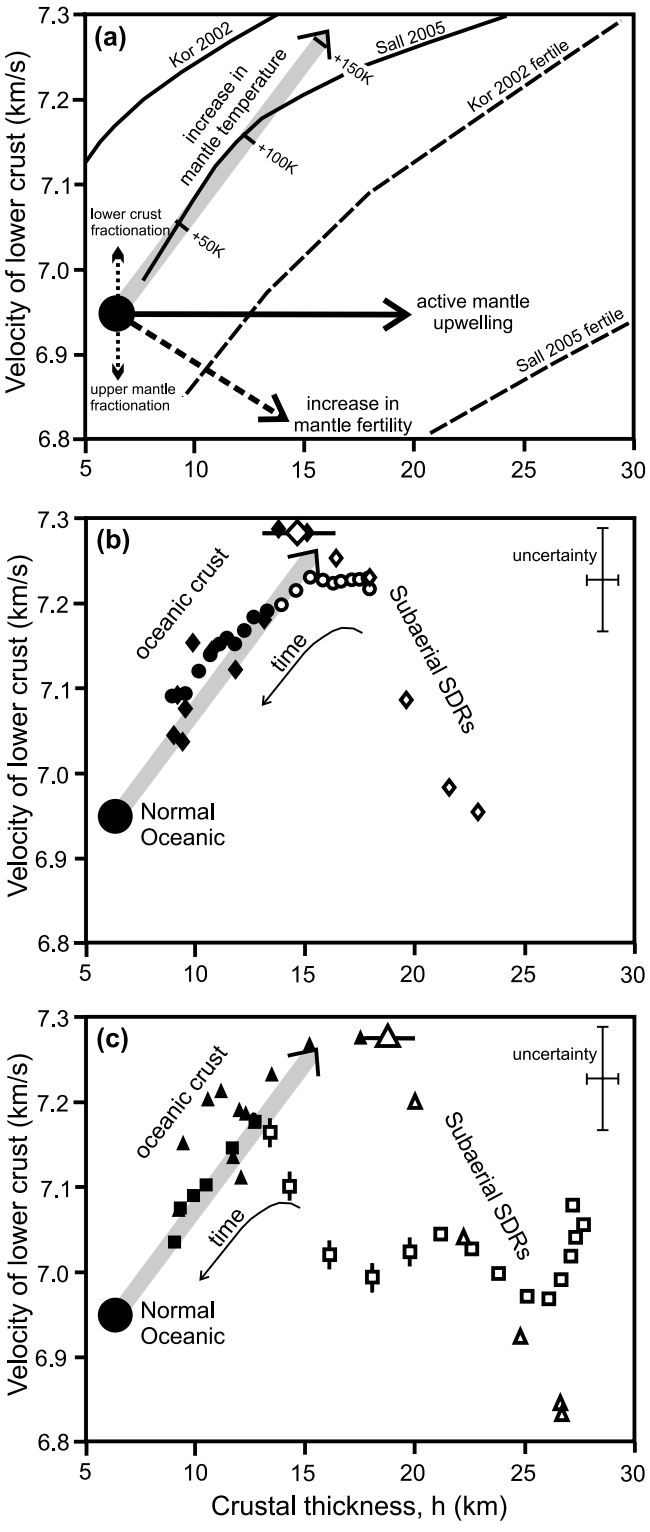

Figure 13. (a) Theoretical igneous crustal thickness versus seismic velocity of primary melts generated by passive mantle upwelling under an oceanic rift calculated by *Korenaga et al.* [2002] and *Sallarès et al.* [2005]: solid lines are from normal pyrolitic mantle, and dashed lines are from fertile mantle. Curves are adjusted to a reference pressure of 230 MPa and a temperature of 150°C, which are representative of conditions in the lower crust of the oceanic data in our results. Filled circle shows the average thickness and lower crustal velocity of normal oceanic crust [*White et al.*, 1992], after correction for along-segment variation in thickness [*Bown and White*, 1994]. Grey shaded arrow shows representative trend of changes in total igneous thickness (h) and lower crustal velocity (V_P) for passive decompression of normal mantle of increasing temperature, with tick marks approximately every 50 K. Large solid arrow and dashed arrow show the directions of h, V_P change at fixed mantle temperature for active mantle upwelling under the rift or an increase in the fertility of the parent mantle, respectively. Small dotted arrows show the effect on the lower crustal velocity of fractionation in the lower crust or in the upper mantle. Redrawn from *White et al.* [2008] (b) Average crustal thickness and lower crustal velocity calculated every 10 km along the iSIMM Hatton dip profile (diamonds, this paper) and the conjugate east Greenland SIGMA-3 profile (circles [*Hopper et al.*, 2003]) after correction to our reference pressure and temperature. Filled symbols are from oceanic crust, and open symbols are from crust lying on the COT beneath arcuate seaward dipping reflector sequences (SDRs). Large open diamond with horizontal uncertainty bar shows the limits of the total (intrusive plus extrusive) igneous thickness across the Hatton COT, with the intrusive igneous volume calculated from the lower crustal velocity using a linear mixing law between lower continental crust and fully igneous oceanic crust. The standard deviations typical of the data points are shown in the top right corner: the theoretical curves have similar uncertainties. Arrow marked "time" shows younging direction of the basalts. (c) The h−v_P data from the Faroes profile (triangles [*White et al.*, 2008]) and the SIGMA-2 profile off Greenland (squares [*Korenaga et al.*, 2000]), both of which lie ~200 km from the center of the Iceland mantle plume thermal anomaly as marked by the flow line on the Greenland-Iceland-Faroe Ridge (Figure 14): filled symbols are from oceanic crust, open symbols from crust beneath SDRs, with the vertical bar through five of the SIGMA-2 values marking points that lie beneath an offshore basement high interpreted here as a dominantly continental block (see text for details).

of a number of limitations on using h-v_p plots to constrain the cause of melting. First is the problem that the theoretical calculations of the seismic velocities that are predicted on h-v_p plots have an uncertainty of about 0.1 km/s for any given melt thickness. Although different authors with slightly different, but equally reasonable assumptions predict different curves, there is a striking consistency in the slopes of the curves which allows us to interpret the causes of analogous trends in our observational results as outlined above [see *Parkin and White*, 2008]. The slopes of the curves are more robust than the absolute values of h and v_p at any particular point, and allow us to infer the magnitude of mantle temperature changes more precisely than absolute mantle temperatures.

[55] The second main difficulty is in defining the v_p of the primary melt. This is partly because the melt itself fractionates in the crust: this has the effect of increasing v_p of the material which freezes in the lower crust, since the main mineral to crystallize out is olivine with a characteristically high seismic velocity, while the basaltic fractionates which are commonly extruded to the surface exhibit lower $v_{p.}$ However, if some of the melt is intruded as sills in the upper mantle and there undergoes some fractionation before moving upward into the crust (as suggested for Icelandic lavas from petrological arguments by *Maclennan et al.* [2001]), then that would have the effect of lowering v_p of the fractionated igneous melt which freezes in the crust. Since these effects change v_p in opposite directions (vertical dotted arrows on Figure 13a), it is likely that at least to some extent they will cancel one another. Another physical effect which makes it difficult to calculate the v_p of primary melt is that, at least in the upper crust, porosity caused by cracks and pore space, and the effects of alteration significantly lower the seismic velocity, generating the characteristic large velocity gradient in the basalts preserved in the upper crust, apparent in the upper 4 km of the velocity-depth profile shown in Figure 10d. A correction to counter this effect implemented by *Korenaga et al.* [2000], by *Holbrook et al.* [2001], and by *Hopper et al.* [2003] was to replace all the upper crustal velocities of less than 6.85 km/s with material of the same thickness with a velocity of 6.85 km/s and then to calculate the harmonic mean of the corrected whole crustal section. *Korenaga et al.* [2002] subsequently suggested that a better approximation to the velocity of the primary melt would be to take the average velocity of just the igneous lower crust below the depth at which a significant change in velocity gradient occurs marking the layer 2–3 boundary in oceanic crust. On our data, this occurs at a velocity of 6.7 km/s (Figure 10d), so we take the average velocity of the lower crust beneath the 6.7 km/s isovelocity contour as representative of the velocity of the primary melt. Since there is a small effect of pressure and temperature on v_p in the crust, we correct all the velocities to an average pressure of 230 MPa and an average temperature of 150°C before calculating their averages.

[56] The third uncertainty in the knowledge of v_p arises from the limits of the tomographic inversion constraints, which typically have standard deviations for uncertainty of the velocity in the lower crust of 0.1 km/s (Figures 7c and 8c). Finally, we assume that all the melt produced at a particular position on the continental margin remains in a vertical column at that position, with no lateral flow.

[57] Having listed all these uncertainties, it is perhaps surprising that there are any coherent trends in our data. But as Figure 13b shows, there are extremely consistent h-v_p trends in the data from oceanic crust adjacent to both the Hatton margin (filled diamonds), and the conjugate Greenland margin (filled circles). Furthermore, the trends point directly toward the average h-v_p value for normal oceanic crust (large filled circle on Figure 13), calculated from a global compilation of crust away from mantle plumes [*White et al.*, 1992] after correction for along-segment variations in thickness [*Bown and White*, 1994]. The trend is precisely that expected from melt generated by passive decompression of mantle at varying temperature rising beneath an oceanic spreading center. Data from oceanic crust adjacent to both the Hatton margin and the conjugate Greenland margin fall on the same trend, and suggest that the mantle temperature beneath this part of the rift decreased by about 70–80°C over the first 10 Ma of seafloor spreading. The Hatton data extend to crust of 38 Ma age, some 5 Ma younger than the Greenland SIGMA-3 data, and the steady decrease in mantle temperature is reflected by the Hatton data (filled diamonds on Figure 13b) extending to slightly lower h and v_p values than does the Greenland data (filled circles on Figure 13b). At the 38 Ma age of generation of the youngest oceanic crust mapped adjacent to the Hatton margin, the inferred mantle temperature was still some 50°C above normal, indicating the continuing widespread influence in the region of the Iceland mantle plume [*White*, 1997].

[58] The criterion used to define the oceanic crustal values marked by filled symbols on Figure 13b is that the crust was submarine at the time of generation and exhibits unambiguous seafloor spreading magnetic anomalies. In practice, on the Hatton and Greenland SIGMA-3 transects the oldest clear seafloor spreading magnetic anomaly is 24 (Figure 14). Crust landward of this anomaly on both the Hatton and Greenland sides exhibits prominent convex-up subaerial seaward dipping reflectors and only small magnetic anomalies (Figure 15). We discuss later the conditions under which the SDRs were generated, and what can be inferred about the underlying crust and mantle, but for the moment will restrict ourselves to unambiguous oceanic crust where the crust is 100% igneous and so the crustal thickness, excluding sediments, is identical to the igneous thickness.

[59] This pattern of decreasing mantle temperature with age of the oceanic crust produced immediately after continental breakup, and predicted from an h-v_p diagram, is also found on other transects in the North Atlantic for which appropriate data are available. Values for h-v_p of oceanic crust from the iSIMM profile northeast of the Faroe Islands in the Norwegian Basin (filled triangles on Figure 13c [from *Parkin and White*, 2008]), fall on the same trend, as also do oceanic data from the Irminger Basin beyond the ''transitional crust'' of the SIGMA-2 profile on the Greenland margin (filled squares on Figure 13c [from *Korenaga et al.*, 2002]). We conclude, with *Barton and White* [1997a], *Holbrook et al.* [2001], and *Hopper et al.* [2003], that the mantle temperature following the onset of seafloor spreading decreased steadily by about 70–80°C over the first 10 Ma of seafloor spreading, and that there is no necessity to invoke mantle convection in areas of oceanic crust formed in the North Atlantic that do not lie directly above

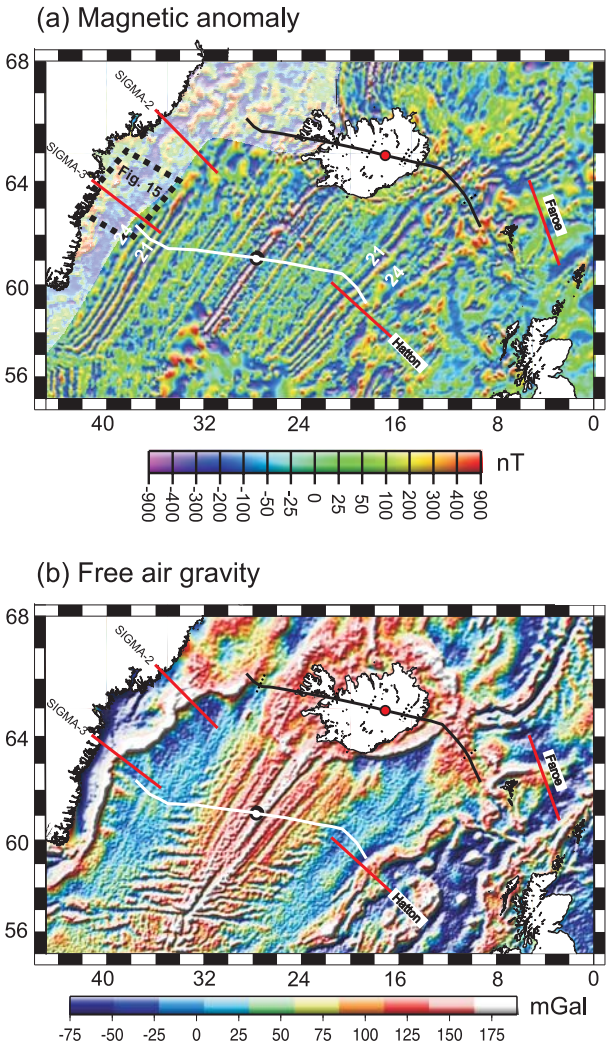

Figure 14. (a) Magnetic anomalies in the northeast Atlantic [*Macnab et al.*, 1995], with flow lines (white and black lines) back to anomaly 24 time centered on the present spreading axis [from *Smallwood and White*, 2002]. Anomalies 21 and 24 are labeled. Note that there have been well-documented ridge jumps on the Icelandic spreading axes, so the black line does not map the entire flow line back to breakup time. Masked area is the region on the Greenland margin where basalts were extruded subaerially [from *Larsen and Saunders*, 1998]. Dotted box marks area of Figure 15 which shows enlargement of the aeromagnetic anomalies. (b) Free air satellite gravity field [*Sandwell and Smith*, 1997] illuminated from the northwest.

the relatively narrow (about 100 km diameter) rising plume core that created the thick crust of the Greenland-Iceland-Faroe Ridge.

6. Conjugate Margin Structure

[60] Our new Hatton profile and the Greenland SIGMA-3 profile are not precisely in conjugate positions. They are separated by about 100 km along strike (Figure 14). However, there is no evidence for major segmentation, ridge jumps or transform faults over this interval so the assumption that the conjugate margins can be reconstructed to investigate their asymmetry is a reasonable one. Earlier reconstructions between the Greenland SIGMA-3 and the older Hatton crustal profiles of *Fowler et al.* [1989] and *Morgan et al.* [1989] have been published by *Hopper et al.* [2003] and by *Smith et al.* [2005]. They show a marked asymmetry, which is also apparent with our new, better controlled data (Figure 16). The two margin profiles in Figure 16 are joined at magnetic anomaly 22 (49 Ma), which is at a time well after mature submarine seafloor spreading had developed in the ocean basin.

[61] It is worth noting the differences in the constraints used to build the models on the two margins. The Hatton model was derived from a total of 49,311 separate traveltime picks recorded at 85 OBS, with the arrivals modeled to an RMS error of 64 ms. On the Greenland SIGMA-3 profile there are more than an order of magnitude fewer picks, totaling 2933, into 19 OBS and 6 shore-based seismometers, and the traveltimes are fitted to "better than 100 ms" in the oceanic part of the profile [*Hopper et al.*, 2003]. The final Hatton model was calculated from an ensemble of 100 inversions with randomized starting models using Tomo2D, whereas the Greenland model was derived by trial and error forward modeling using Rayinvr. However, the conjugate profiles are broadly similar in their resolution, which means that we can draw robust conclusions about the main large-scale structure.

[62] There are two obvious asymmetric aspects to the conjugate profiles shown in Figure 16. The first is the continental hinterland. On the Greenland side the continental crust attains a greater thickness than on the Hatton side: over 30 km thick under Greenland compared to only 23 km for the maximum thickness under Hatton Bank. Quite possibly the Greenland crust gets thicker still into the Greenland craton farther away from the coast, but the SIGMA-3 profile does not constrain it that far. Consistent with the differences in crustal thickness, most of the Greenland continental crust has its surface above water, whereas all of Hatton Bank is below sea level. This marked difference is because the Hatton side had undergone earlier Mesozoic stretching and Hatton Bank itself is backed by the stretched Hatton Basin, and the still more stretched Rockall Basin. It is interesting that the ultimate continental breakup did not reoccupy one of these earlier Mesozoic rifts but instead occurred at the edge of them, along the margin of the Archean Greenland craton. Similar behaviors are seen elsewhere along the European-Greenland breakup, suggesting that the processes involved in the Mesozoic stretching and subsequent lithospheric equilibration on the European margin left the lithosphere locally stronger than on the Greenland side, which had not undergone that prior stretching. Although there is asymmetry in the continental thickness of the hinterland, the seismic velocities of the continental crust beneath Hatton Bank and Greenland are similar, which is to be expected since they were originally part of the same continental block, presumably with similar and contiguous geological structure.

6.1. Asymmetry of Crust With Seaward Dipping Reflectors

[63] The most obvious asymmetry between the two flanks of the North Atlantic rift is in the sections of crust exhibiting

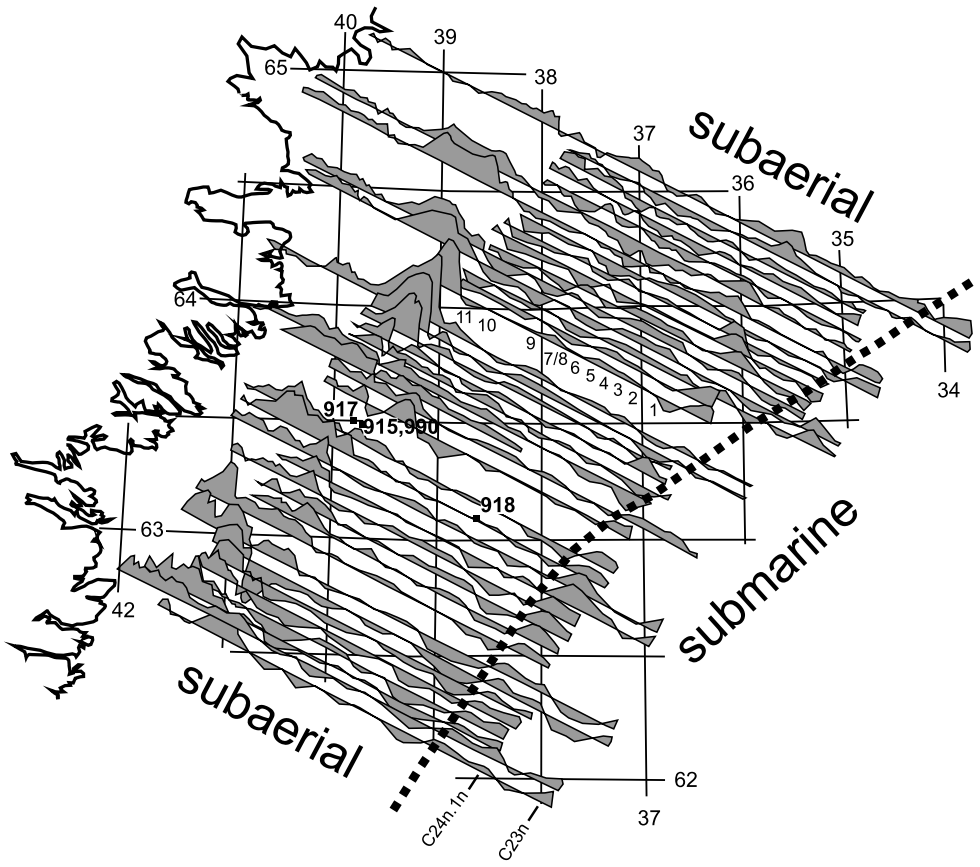

Figure 15. Enlargement of aeromagnetic anomalies on east Greenland shelf from *Larsen and Thorning* [1979] (see Figure 14 for location). Small numbers 1–11 mark the interpretation from *Larsen et al.* [1994a, 1994b] and *Larsen and Saunders* [1998] of small-amplitude cryptochrons during anomaly C25r. The boundary between subaerial (landward side) and submarine Tertiary lavas shown by dashed line is from *Larsen and Saunders* [1998]. In this paper we suggest that the inferred cryptochrons are artifacts caused by subaerial flow fronts and variations in the subaerial basalts and do not represent seafloor spreading magnetic anomalies, with the consequence that very high and asymmetric spreading rates are not required during this interval. Numbers 915–918 and 990 mark ODP drill holes that penetrated significant volcanic sequences. Note that in the original diagrams published by *Larsen et al.* [1994a, 1994b] and *Larsen and Saunders* [1998] the lines of longitude are mislabeled and the coastline is not the right position: both have been corrected in this redrafted plot.

well-formed convex-up SDRs (i.e., 90–190 km on the Greenland margin, versus 70–110 km on the Hatton Margin, Figure 16). The SDRs in these intervals on both sides of the Atlantic have been interpreted as caused by lava flows extruded subaerially, a conclusion supported by samples taken from ODP drilling [*Larsen and Saunders*, 1998; *Hopper et al.*, 2003]. The magnetic spreading anomalies also change character from the prominent anomalies 24 and younger generated in submarine settings to only indistinct anomalies where the basalt flows were extruded subaerially in the region of SDRs (see shaded area on Figure 14a). The normal explanation for the prominent asymmetry is that there was grossly asymmetric seafloor spreading, or a continuously migrating ridge axis, with the Greenland side spreading at a half rate of about 44 mm/a between 55 and 53 Ma, about three times faster than the half spreading rate of 15 mm/a on the Hatton side [*Larsen and Saunders*, 1998]. Though this is an uncomfortable conclusion because there are no other known cases of such a high ratio of asymmetric oceanic spreading rates it is clear, as *Hopper et al.* [2003] point out, that the continuous nature of the SDRs preclude the possibility of ridge jumps being invoked to explain the asymmetry.

[64] However, we show here that the basis on which the spreading rate on the Greenland side is calculated may in fact be incorrect, even though at first sight it appears to be based both on the identification of seafloor spreading magnetic anomalies and on dating of basalts from ODP holes. We show that these same data can also be interpreted as supporting a model with similar seafloor spreading rates on both flanks of the new oceanic rift, which is more in keeping with normal seafloor spreading processes. This then raises the interesting corollary that the initial continental stretching (rather than the subsequent seafloor spreading), was highly asymmetric, as is often observed on nonvolcanic continental margins elsewhere, and that the subsequent magmatism simply inherited and filled this existing asymmetrically stretched continental crustal structure. It also has ramifications in how we interpret h-v_p diagrams, removing the need for the counterintuitive interpretation made by

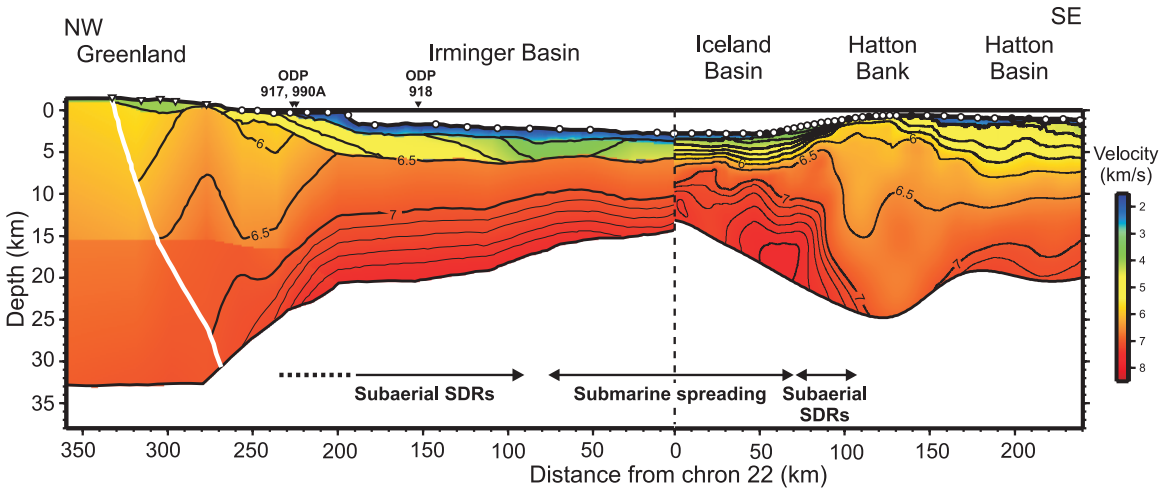

Figure 16. Comparison of velocity models from the iSIMM Hatton profile (this paper) and the SIGMA-3 east Greenland conjugate profile [*Hopper et al.*, 2003]. The locations of ODP Leg 152 drill sites 917, 918, and 990A are marked by filled triangles. OBS locations marked by open circles, land stations by open triangles. Models are aligned at chron 22. Contours are drawn every 0.5 km/s from 3.5 to 7.0 km/s and every 0.1 km/s for velocities >0.1 km/s. White line marks the limit of ray coverage in the SIGMA-3 velocity model.

Korenaga et al. [2002] that immediately after continental breakup the mantle temperature was relatively cool, but with highly active mantle convection required to generate the thick igneous section, and that this was followed during the early seafloor spreading by a gradual increase in mantle temperature accompanied by subsidence, a decrease in active convection, and a decrease in the seafloor spreading rate.

[65] The crux of the spreading rate argument comes from identification of seafloor spreading magnetic anomalies. On both sides of the ocean basin, prominent anomalies 19, 21, 22, and 24 are readily identifiable (Figure 14a). The half spreading rate deduced from chron 24 to chron 21 time on both sides of the basin is about 15 mm/a, decreasing to a half rate of about 10 mm/a after chron 21 [*Smallwood and White*, 2002]. A higher initial spreading rate immediately following continental breakup is found throughout the North Atlantic, including areas north of Iceland [e.g., *Voss and Jokat*, 2007]. However, although anomaly 24 lies close to the break of slope on the Hatton margin, on the Greenland margin it lies more than 100 km seaward of it. In the interval between anomaly 24 and the coast, a series of faint, sinuous lineations on the Greenland margin mapped by an aeromagnetic survey have been interpreted by *Larsen et al.* [1994a, 1994b] and *Larsen and Saunders* [1998] as representing cryptochrons 24.1n to 24.11n within reversed anomaly 24r (Figure 15). These 11 cryptochrons span an age of only 1.8 Ma, but are identified over a downdip distance of 80 km, so this interpretation leads to a very high half spreading rate of 44 mm/a off the Greenland margin.

[66] An alternative, and in our opinion a more likely explanation of these faint aeromagnetic lineations is that they represent the edges of subhorizontal lava flows which flowed in a landward direction across the then subaerial shelf. So they cannot be interpreted as seafloor spreading anomalies. Indeed in the northern part of the data shown in Figure 15 the sinuous nature of some of the anomalies is reminiscent of flow fronts. These anomalies interpreted as cryptochrons all lie in a region that was subaerial at the time the basalts were emplaced (Figures 14a and 15). *Smallwood et al.* [2001] have shown from an analogous geological setting on the Faroes shelf that lineated magnetic anomalies can be modeled by the termination of subhorizontal basalt flows. The subaerial flows on the Faroes shelf extend over 150 km from the rift, and are of the same age and in a similar geological setting to the flows off east Greenland. Not only is it likely that the faint magnetic lineations off Greenland are caused by the terminations of individual subaerial basalt flows, but the alternative explanation that they represent consistently laterally restricted, typically 5- to 10-km-wide zones of alternately magnetically polarized igneous rocks emplaced in situ, as required if they were really seafloor spreading anomalies, is extremely unlikely in this highly volcanic, subaerial, flat-lying area where basalts could flow laterally many tens of kilometers.

[67] The other evidence for the dating on the Greenland margin comes from ODP borehole samples. There is only one dated basalt in the interval with SDRs landward of anomaly 24, which comes from hole 918 (see Figures 15 and 16 for location), and unfortunately the constraints on this date are rather poor, at 54.0 ± 1.8 Ma [*Larsen and Saunders*, 1998]. Also, of course, these basalts may have flowed long distances laterally in a landward direction as the fissures from which the basalts came were not located at the position of hole 918: *Larsen and Saunders* [1998] comment that the basalt may have flowed 20–30 km downdip from the rift, and we consider this a minimum. A sill 9.3 m above the volcanic basement in the overlying sediments has an Ar–Ar age of 51.9 Ma [*Sinton and Duncan*, 1998], and probably intruded down into unconsolidated sediments from the rift to seaward during chron 23r or younger [*Larsen and Saunders*, 1998]. Other than the hole 918 dates, there are several dates from samples of basalts at least 600 m thick in ODP hole 917 found in fault

blocks on the continental margin (see Figures 15 and 16 for location), which generally give much older ages of 62–60 Ma for subaerially, continentally contaminated lavas [*Sinton and Duncan*, 1998]. The volcanism at this continental site is found within tilted fault blocks and is likely therefore not to have flowed long distances laterally at the surface because there was probably considerable paleotopography that would have inhibited that, and is underlain by continental crust. Slightly seaward of hole 917, at ODP hole 990A, which also penetrated a tilted fault block, younger ages of 55.7 ± 0.5 Ma are reported in basalts with evidence of only slight continental contamination [*Tegner and Duncan*, 1999]. This is at the feather edge of the SDRs and these lavas may have flowed from an oceanward rift.

[68] We conclude that there is no requirement from the magnetic anomaly data and basalt ages for the extremely high half rate of seafloor spreading off the Greenland margin that has previously been inferred from the small aeromagnetic anomalies and the concomitant assumed asymmetric seafloor spreading older than anomaly 24. As we show in the next section, we suggest that the asymmetric crust apparent in Figure 16 is likely to be underlain by stretched and intruded continental crust rather than fully oceanic crust, so it is more likely that the asymmetry is caused by the initial continental stretching than by the subsequent seafloor spreading.

6.2. Nature of the Crust Beneath Seaward Dipping Reflectors

[69] A crucial question concerns what constraints can be placed on the nature of the crust beneath the SDRs. *White et al.* [2008] have argued from the seismic data on the European margins of the North Atlantic that the h-v_p plots are consistent with the intrusion of high-velocity igneous sills into continental crust with lower seismic velocities across a narrow (~40 km wide) continent-ocean transition zone, which separates continental crust from fully oceanic (i.e., fully igneous) crust. The effect of lower crustal igneous intrusion into continental crust is to produce average velocities sampled by wide-angle seismic arrivals that are intermediate between the velocities of the continental crust and those of the fully igneous oceanic crust.

[70] We take as the best estimate of the seismic velocity of the igneous intrusions in the COT the velocity of the lower crust at the location of the oldest oceanic crust. Using the continental velocity-depth profile (Figure 10b) as one end-member, with the velocity of the earliest ocean crust (Figure 10d) as the other, then the lower crustal igneous volume under the COT can be calculated from the average velocity using a linear mixing law. Combined with the extrusive basalt volume, this gives an igneous thickness averaged across the COT of 13–16 km (plotted as large open diamond on Figure 13b), which falls on the linear h-v_p trend that is consistent with melt formation by decompression of abnormally hot mantle rising passively beneath the lithospheric rift formed at the position of continental breakup. The inferred mantle temperature on this interpretation decreases from a maximum at the time of continental breakup through the succeeding 10 Ma of seafloor spreading. There is the possibility in this calculation of some trade-off between the assumed velocity of the intruded igneous sills under the COT and their thickness: if the intrusions were of lower seismic velocity than the first-formed oceanic crust (and therefore probably formed from lower temperature mantle), then their inferred thickness would be greater. This would then allow the inference of limited small-scale mantle convection to generate the melt thickness, since they would have lower v_p and greater h. But even if this were so, modeling of the North Atlantic margin development by *Nielsen and Hopper* [2002] suggests that increased mantle temperatures are still required.

[71] A break in the slope of the h-v_p points on the conjugate east Greenland arrivals from the SIGMA-3 profile is also apparent at approximately the location of the change from crust with convex arcuate SDRs interpreted as formed subaerially (90–190 km on Figure 16, open circles on Figure 13b) to younger submarine oceanic crust (of age chron 24 and younger, filled circles on Figure 13b). By analogy with the h-v_p values from the Faroes profile, this suggests that there is a small amount of continental crust present under the subaerially formed SDRs, which serves to lower the crustal velocities somewhat below what they would be if the crust were fully igneous.

7. Other North Atlantic Continental Margin Transects

[72] There are two other well-constrained crustal velocity profiles across the North Atlantic margins that can be used to extract h-v_p values in the same way as discussed in section 6 (SIGMA-2 and Faroes profiles, Figure 14). They lie on opposite sides of the North Atlantic, and both are ~200 km from the center of the Iceland mantle plume trace marked by the Greenland-Iceland-Faroe Ridge of thick crust (black flow line, Figure 14). However, they are not strictly conjugate profiles because the Faroes profile [*White et al.*, 2008] lies to the north of the mantle plume trace, while the SIGMA-2 profile [*Korenaga et al.*, 2000] lies to the south of it.

[73] As shown in Figure 13c, the h-v_p pattern from the Faroes profile (triangles) is closely similar to that from the Hatton profile shown in Figure 13b. There is a break in slope of the values from submarine oceanic crust which are consistent with passive decompression beneath an oceanic spreading center (filled triangles), to those from beneath arcuate subaerial SDRs on the narrow continent-ocean transition (open triangles). Following the same procedure of using a linear mixing law between the seismic velocity of the lower crustal igneous intrusions inferred from the oldest fully oceanic crust and the velocity of the adjacent continental crust yields an average igneous crustal thickness across the COT of 18–20 km (large open triangle and error bar on Figure 13c), which is equivalent to the emplacement of ~900–1000 km^3 of igneous rock per kilometer along strike.

[74] The SIGMA-2 profile yields a not dissimilar h-v_p pattern to that seen on the Faroes and Hatton profiles, with a distinct break in slope between the points from oceanic crust (filled squares on Figure 13c), and that termed transitional crust by *Korenaga et al.* [2000] (open squares on Figure 13c). The transitional crust is complicated by an offshore basement block imaged by a seismic reflection profile [*Korenaga et al.*, 2000, Figure 3] that divides the fully oceanic crust from a region of well-developed SDRs

adjacent to the continental block: the h-v_p points from the SDR section are shown by open squares on Figure 13c, while those above the basement block are marked by a vertical line through the open square. The precise values of v_p on Figure 13c are slightly different from those shown on an analogous diagram by *Korenaga et al.* [2000, Figure 14], because we have used the velocity of just the lower crust and have corrected the velocities to our reference pressure of 230 MPa and a temperature of 150°C: the differences are only minor and the pattern remains the same. *Korenaga et al.* [2000] interpreted the transitional crust as being formed from mantle with a temperature only ~50°C above normal, so in order to produce the large thicknesses they required active mantle convection well over 8 times and probably in excess of 16 times the passive upwelling rate. Since they infer that the mantle temperature did not change much (the points are subhorizontal on the h-v_p diagram), it follows that the degree of active convection must have decreased as the transitional crust was formed with decreasing thickness until anomaly 21 time when normal oceanic crust was generated (at which point the symbols on Figure 13c change to filled squares). This conclusion is quite different from those we have reached from the other seismic profiles in the region.

[75] We present here an alternative explanation that is consistent with the other three continental margin profiles discussed in sections 6 and 7. If there is a component of stretched continental crust beneath the 100-km-wide transition zone on the SIGMA-2 profile, then the measured velocities of the lower crust would be a mixture of the velocities of the continental crust and the higher velocity igneous intrusions. High-temperature igneous intrusions would be consistent with the presence of high-temperature mantle beneath the region at the time of stretching, which then cooled over the next 10 Ma of seafloor spreading following continental breakup. The oldest identifiable seafloor spreading anomaly in this region crossed by the SIGMA-2 profile is anomaly 21 (Figure 14a), which coincides with the first fully oceanic crust (filled square) identified on Figure 13c: *Korenaga et al.* [2000] extrapolated anomalies 22–24 from the adjacent region across the transitional crust, but as Figure 14a shows, there is an abrupt termination of those anomalies south of the SIGMA-2 transect. So that extrapolation is unsafe. That is not to say, of course, that igneous material formed during chrons 22–24 is absent: rather, if this region was subaerial, then we would not expect clear seafloor spreading magnetic anomalies to be present anyway. But in addition, there is a large embayment in the conjugate margins in the region which the SIGMA-2 profile traverses, which is visible in the magnetic anomalies (Figure 14a), and even more clearly in the gravity anomaly map (Figure 14b). This requires a transform fault across the margin south of SIGMA-2, and there may also be a ridge jump here, as *Smallwood and White* [2002] postulate. So again it seems likely that there is highly stretched continental crust underlying the extrusive basalts that form the SDRs above the transitional crust on the SIGMA-2 profile.

[76] The added complication in the case of the SIGMA-2 profile is the 50-km-wide basement high that separates the oceanic crust from the crust with subaerial SDRs. The explanation we favor is that it comprises a block of continental crust separated from the Greenland mainland by more extended continental crust, and so was elevated more than the intervening region at the time of breakup. The SDRs terminate against it, in a manner identical to that reported from the Edoras Bank margin by *Barton and White* [1997b]. Isolated continental blocks separated by more stretched crust are common throughout the northern North Atlantic region, including, among other things, Rockall Bank, Hatton Bank, Lousy Bank, Edoras Bank and the Faroes Bank. By the time normal seafloor spreading was developed at chron 21, the mantle temperature had cooled by ~50°C from the highest temperatures recorded on the Hatton and Faroes profiles, and the h-v_p point at chron 21 reflects this by joining the oceanic array of points part way down the array at a somewhat cooler temperature, which nevertheless is still well above normal mantle temperatures (Figure 13c).

8. Underplating or Lower Crustal Intrusion?

[77] Much of our geological interpretation of the high-velocity lower crust (HVLC) discussed in this paper is predicated on the assumption that it represents continental crust heavily intruded by igneous rocks (probably primarily as sills), rather than a block of 100% igneous rock underplated beneath the preexisting crust. If the HVLC represents underplated melt, then the h-v_p plots require active convection of relatively low temperature mantle during the formation of the earliest oceanic or transitional crust seaward of the continent-ocean boundary, followed by first an increase in mantle temperature, peaking at chron 24 time, with a concomitant reduction in active convection, then a decrease in mantle temperature as oceanic crust was generated after chron 24. The alternative model, which we prefer, is that the HVLC beneath the subaerial seaward dipping reflectors represents continental crust intruded by igneous sills, from which the h-v_p points are consistent with the mantle temperature being at a maximum at the time of continental breakup, and then decreasing monotonically thereafter.

[78] The evidence for the melt being intruded rather than underplated comes first from the subhorizontal reflectivity interpreted as sills in the lower crust that is imaged beneath the COT on the Faroes margin and is coincident with the region of the HVLC [*White et al.*, 2008]. Second, igneous dykes generated in large igneous provinces have frequently been mapped extending large distances from their sources, showing that melt intrusion as relatively thin bodies in the lower continental crust does occur geologically [*Ernst and Buchan*, 2001].

[79] It is instructive to review briefly the use of the term underplating on volcanic margins, since such terminology often governs the conscious or subconscious interpretations one makes. The suggestion that basaltic igneous provinces are likely to contain fractionated products in the underlying crust first came from petrological arguments [e.g., *O'Hara*, 1965; *Thompson*, 1974]. *Cox* [1980] argued that if parental lavas under flood basalt provinces were picritic, then they must have intruded the base of the crust as a series of sills which then underwent low-pressure fractionation to produce basaltic magmas, leaving the sills differentiated into upper gabbroic and lower ultramafic portions. He explicitly stated that a new seismic Moho would then be generated at the boundary between the differentiated ultramafic layer and the gabbroic layer, although acknowledging that multiple injec-

tions of primitive melt would generate a diffuse Moho boundary. In this model, *Cox* [1980] comments that the volume of material added to the base of the crust is likely to be at least as large as the volume of extrusive basalts, a finding supported by our seismic results. Although clear in his description of the difference between the ultramafics below the Moho and the gabbroic sill injections in the crust, in a later paper, *Cox* [1993, p. 155] wrote that all the magmas ''trapped at or near the Moho, or within the crust, or in complex crust-mantle transition zones'' were known as underplating. So already this terminology of the location of igneous material, whether injected into the crust or accumulated as a solid layer at its base, was blurred.

[80] Careful petrological analysis shows that it is sometimes possible to track the stages at which melt has paused and partially fractionated on its journey to the surface: *Maclennan et al.* [2001] have shown that beneath Iceland, melt is at least temporarily trapped both in upper mantle and lower crustal sills, and *Thompson et al.* [2007] postulate multiple lower crustal sills beneath the Etendeka flood basalt province.

[81] A second area of study which suggested that some melt was trapped in or beneath the crust was subsidence (and uplift) analysis. Writing about possible mechanisms of epeirogenic uplift, *McKenzie* [1984, p. 616] proposed that it could be caused by the ''intrusion of large thicknesses of basic magma into the lower part of [the] continental crust'', envisaging this either as sills in the continental crust or as a layer between the crust and the mantle if its density were intermediate between them. The uplift calculations are not sensitive to whether new igneous material is intruded into the lower crust or upper mantle, and many subsequent papers have simply considered added melt as underplated without necessarily implying that it was therefore a layer of 100% igneous rock rather than sills [e.g., *Brodie and White*, 1994; *White and Lovell*, 1997; *Rowley and White*, 1998; *Maclennan and Lovell*, 2002].

[82] The third area of usage is in seismic experiments, and here it really does matter whether the new igneous material is intruded as sills or is underplated, for the interpretational reasons of h-v_p systematics discussed earlier. An important early paper by *Furlong and Fountain* [1986] discussed the addition of igneous material to the base of the crust, particularly in rifted regions, and the seismic signature it would produce. Although *Furlong and Fountain* [1986, p. 8290] do mention that melt might be intruded as sills in the lower crust and thus ''result in a laminated structure which may be interpreted as a ''laminated'' moho'', the thrust of the paper assumes that the melt accumulates as a solid layer up to 10 km or more thick beneath or at the base of the crust.

[83] A seminal paper on the crustal structure of the East coast margin of the United States published in the same year [*LASE Study Group*, 1986], involving people from many of the major North American oceanographic institutes, detected the presence of a HVLC layer extending beneath the continental margin continuously to the lower part of the adjacent oceanic crust: this was interpreted as underplated igneous material. Writing about the HVLC mapped on the Hatton margin, *White et al.* [1987, p. 441] were more diffident in their interpretation, commenting that ''from the seismic evidence alone we cannot tell whether the lower crust comprises a relatively uniform layer of rock underplated beneath the upper crust or heavily intruded preexisting material'' while *White* [1987, p. 191], reporting on a conference discussing Tertiary volcanism and the opening of the NE Atlantic wrote that ''between the unstretched, continental crust and the new, oceanic crust there must be a region where the percentage of igneous rock in the crust increases due to both intrusion and extrusion''. In a subsequent review of large igneous provinces, *Coffin and Eldholm* [1994] cautioned that they considered the term ''underplating'' a misnomer, because it implies that the new melt is trapped by a density difference between the crust and the mantle. A number of other authors have been careful to use the nongenetic term HVLC rather than referring to underplating.

[84] Nevertheless, many authors then went on to assume that the HVLC indeed comprised 100% new igneous rock rather than intruded lower crust, even if they did not explicitly use the term underplating [e.g., *Kelemen and Holbrook*, 1995; *Holbrook et al.*, 2001; *Korenaga et al.*, 2002]. Others simply interpreted the HVLC as magmatic underplating without discussion [e.g., *Mutter et al.*, 1984; *Larsen and Saunders*, 1998; *Vogt et al.*, 1998; *Geoffroy*, 2005; *Klingelhöfer et al.*, 2005; *Voss and Jokat*, 2007]. We conclude that though it does not matter greatly for subsidence analysis, the semantics of the models play an important, if sometimes unconscious role in governing the interpretations made from systematic h-v_p variations across volcanic rifted margins. We suggest that the term underplated be reserved to describe circumstances where the HVLC is interpreted as definitely comprising 100% new igneous rock accumulated beneath the preexisting crust but otherwise to use a nongenetic term such as HVLC, or else to make it clear that the high velocities may be due either to underplating sensu stricto or to intrusion into the lower crust.

9. Conclusions

[85] Dense OBS coverage on a dip and strike profile across the Hatton rifted continental margin in the North Atlantic has enabled us to place good constraints on the velocity structure of the continent-ocean transition, extending well into the oceanic crust on one side and the continental hinterland on the other. Tomographic inversion from 100 randomized starting models provide robust measures of the velocities and their uncertainty at all points across the model.

[86] We show that the continent-ocean transition off Hatton Bank is surprisingly narrow: the lower crustal velocity structure changes from continental to fully oceanic in a distance of only ~40 km downdip. The injection of mantle melts at temperatures well above the melting point of the continental crust is postulated to have weakened it sufficiently to cause subsequent stretching and breakup to become focused at the location of the narrow COT.

[87] Interpretation of h-v_p systematics shows that the velocities of the lower crust across the COT can be modeled by the injection of igneous
melts from mantle that had a maximum temperature of ~120–130°C above normal at the time of continental breakup at ~56 Ma, and then decreased by ~70–80°C

over the next 10 Ma of seafloor spreading. This simple scenario does not require postulating vigorous mantle convection beneath the rift of relatively low-temperature mantle, nor does it require the presence of fertile mantle at the time of continental breakup. It is not possible to discriminate from the observations between models of passive decompression beneath the rift or models with a maximum mantle temperature a few tens of °C lower with modest mantle convection at breakup time, but elevated mantle temperatures of the order of at least 100°C are required in either case. Mantle temperature anomalies with a maximum of 120–130°C above normal are consistent with temperature anomalies deduced from olivine-liquid equilibria in contemporary ocean islands igneous rocks [*Putirka*, 2008], which are presumed to lie above mantle plumes, and are similar to temperature anomalies inferred from other flood basalt provinces [*White and McKenzie*, 1995].

[88] The conjugate margins off the Greenland margin show a rather different structure than the Hatton and Faroes margins on the European side. Whereas the European COT is very narrow (~40 km), the Greenland transitional crust is rather broad, typically 100 km or more wide. Although this asymmetry of the Greenland margins has been interpreted as representing extremely rapid and asymmetric seafloor spreading with a concomitant requirement that there be rapid mantle convection beneath the rift at a rate of more than 8 times passive upwelling, and with only modest mantle thermal anomalies, we suggest an alternative interpretation that the transitional zone off Greenland contains stretched continental crust. As we show from h-v_p plots, the mantle thermal history would then be the same as that inferred from the European side, with a simple history of monotonically decreasing mantle temperatures following continental breakup. Tilted fault blocks are much more prominent, and some are still present on the Greenland side, and were formed prior to the main phase of volcanism which started at ~55Ma. We suggest that an initial phase of stretching created asymmetric stretched continental crust similar to that reported from nonvolcanic margins [*Chian et al.*, 1995; *Louden and Chian*, 1999], and that this was then buried by the extensive volcanism which created prominent subaerial SDRs as breakup occurred. The reason for the asymmetry may lie in the fact that the European continental hinterland had already been affected by repeated Mesozoic stretching events prior to the Tertiary breakup. This may have strengthened the lithosphere such that the eventual continental stretching and final breakup occurred in the hitherto unstretched region off present-day Greenland on the western side of the Mesozoic regions of extension on the European side.

[89] **Acknowledgments.** The iSIMM project was supported by Liverpool and Cambridge Universities, Schlumberger Cambridge Research Ltd., Badley Geoscience Ltd, WesternGeco, Amerada Hess, Anadarko, BP, ConocoPhillips, ENI UK, Statoil, Shell, the Natural Environment Research Council, and the Department of Trade and Industry. OBS were provided by Geopro GmbH. The iSIMM team comprises N. J. Kusznir, R. S. White, P. A. F. Christie, A. M. Roberts, D. Healy, R. Spitzer, A. Chappell, J. D. Eccles, R. Fletcher, N. Hurst, Z. Lunnon, C. J. Parkin, A. W. Roberts, L. K. Smith and V. J. Tymms. We are grateful to Nick Kusznir for his work as Chief Scientist on RRS *Discovery* during the cruise which collected data on which this paper is based and to the officers, crew, scientists, and technicians on the cruise. John Hopper provided a helpful review, and we are grateful to Peter Clift, Hans Christian Larsen, and Andy Saunders, who confirmed that the coastline and longitudes of the redrafted Figure 15 of this paper were incorrect in their originally published version, as detailed in the Figure 15 caption. Department of Earth Sciences, Cambridge contribution ES9338.

References

Barton, A. J., and R. S. White (1997a), Crustal structure of the Edoras Bank continental margin and mantle thermal anomalies beneath the North Atlantic, *J. Geophys. Res.*, *102*, 3109–3129, doi:10.1029/96JB03387.

Barton, A. J., and R. S. White (1997b), Volcanism on the Rockall continental margin, *J. Geol. Soc.*, *154*, 531–536, doi:10.1144/gsjgs.154.3.0531.

Bown, J. W., and R. S. White (1994), Variation with spreading rate of oceanic crustal thickness and geochemistry, *Earth Planet. Sci. Lett.*, *121*, 435–449, doi:10.1016/0012-821X(94)90082-5.

Brenders, A. J., and R. G. Pratt (2007), Efficient waveform tomography for lithospheric imaging: Implications for realistic, two-dimensional acquisition geometries and low-frequency data, *Geophys. J. Int.*, *168*, 152–170, doi:10.1111/j.1365-246X.2006.03096.x.

Brodie, J., and N. White (1994), Sedimentary basin inversion caused by igneous underplating—Northwest European continental shelf, *Geology*, *22*, 147–150, doi:10.1130/0091-7613(1994)022<0147:SBICBI>2.3.CO;2.

Bunch, A. W. H. (1979), A detailed seismic structure of Rockall Bank (55°N, 15°W): A synthetic seismogram analysis, *Earth Planet. Sci. Lett.*, *45*, 453–463, doi:10.1016/0012-821X(79)90144-4.

Campbell, I. H. (2007), Testing the plume theory, *Chem. Geol.*, *241*, 153–176, doi:10.1016/j.chemgeo.2007.01.024.

Cerveny, V., and J. Psencik (1979), Ray amplitudes of seismic body waves in laterally inhomogenous media, *Geophys. J. R. Astron. Soc.*, *57*, 91–106.

Chapman, C. H., and R. Drummond (1982), Body wave seismograms in inhomogeneous media using Maslov asymptotic theory, *Bull. Seismol. Soc. Am.*, *72*, 5277–5317.

Chian, D., C. Keen, I. Reid, and E. Louden (1995), Evolution of nonvolcanic rifted margins: New results from the conjugate margins of the Labrador Sea, *Geology*, *23*, 589–592, doi:10.1130/0091-7613(1995)023<0589:EONRMN>2.3.CO;2.

Coffin, M. F., and O. Eldholm (1994), Large igneous provinces: Crustal structure, dimensions, and external consequences, *Rev. Geophys.*, *32*, 1–36, doi:10.1029/93RG02508.

Cox, K. G. (1980), A model for flood basalt vulcanism, *J. Petrol.*, *21*, 629–650.

Cox, K. G. (1993), Continental magmatic underplating, *Philos. Trans. R. Soc. London, Ser. A*, *342*, 155–166, doi:10.1098/rsta.1993.0011.

Eccles, J. D., R. S. White, A. W. Roberts, P. A. F. Christie, and the iSIMM Team (2007), Wide angle converted shear wave analysis of a North Atlantic volcanic rifted continental margin: Constraint on sub-basalt lithology, *First Break*, *25*(10), 63–70.

Eldholm, O., and K. Grue (1994), North Atlantic volcanic margins: Dimensions and production rates, *J. Geophys. Res.*, *99*, 2955–2988, doi:10.1029/93JB02879.

Ernst, R. E., and K. L. Buchan (2001), The use of mafic dyke swarms in identifying and locating mantle plumes, in *Mantle Plumes: Their Identification Through Time*, edited by R. E. Ernst and K. L. Buchan, Spec. Pap. Geol. Soc. Am., *352*, pp. 247–265.

Foucher, J.-P., X. Le Pichon, and J.-C. Sibuet (1982), The ocean-continent transition in the uniform lithospheric stretching model: Role of partial melting in the mantle, *Philos. Trans. R. Soc. London, Ser. A*, *305*, 27–43, doi:10.1098/rsta.1982.0024.

Fowler, S. R., R. S. White, G. D. Spence, and G. K. Westbrook (1989), The Hatton Bank continental margin II. Deep Structure from two-ship expanding spread seismic profiles, *Geophys. J. Int.*, *96*, 295–309, doi:10.1111/j.1365-246X.1989.tb04452.x.

Fuchs, K., and G. Muller (1971), Computation of synthetic seismograms with the reflectivity method and comparison with observations, *Geophys. J. R. Astron. Soc.*, *23*, 417–433.

Furlong, K. P., and D. M. Fountain (1986), Continental crustal underplating: Thermal considerations and seismic-petrologic consequences, *J. Geophys. Res.*, *91*, 8285–8294, doi:10.1029/JB091iB08p08285.

Geoffroy, L. (2005), Volcanic passive margins, *C. R. Geosci.*, *337*, 1395–1408, doi:10.1016/j.crte.2005.10.006.

Hitchen, K. (2004), The geology of the UK Hatton-Rockall margin, *Mar. Pet. Geol.*, *21*, 993–1012, doi:10.1016/j.marpetgeo.2004.05.004.

Holbrook, W. S., et al. (2001), Mantle thermal structure and active upwelling during continental breakup in the North Atlantic, *Earth Planet. Sci. Lett.*, *190*, 251–266, doi:10.1016/S0012-821X(01)00392-2.

Hopper, J. R., T. Dahl-Jensen, W. S. Holbrook, H. C. Larsen, D. Lizarralde, J. Korenaga, G. M. Kent, and P. B. Kelemen (2003), Structure of the SE Greenland margin from seismic reflection and refraction data: Implications for nascent spreading center subsidence and asymmetric crustal

accretion during North Atlantic opening, *J. Geophys. Res.*, *108*(B5), 2269, doi:10.1029/2002JB001996.
Joppen, M., and R. S. White (1990), The structure and subsidence of Rockall Trough from two-ship seismic experiments, *J. Geophys. Res.*, *95*, 19,821–19,837, doi:10.1029/JB095iB12p19821.
Kelemen, P. B., and W. S. Holbrook (1995), Origin of thick, high-velocity crust along the U.S. East Coast margin, *J. Geophys. Res.*, *100*, 10,077–10,094, doi:10.1029/95JB00924.
Keser Neish, J. (1993), Seismic structure of the Hatton-Rockall area: An integrated seismic modelling study from composite datasets, in *Petroleum Geology of Northwest Europe: Proceedings of the 4th Conference*, edited by J. R. Parker, pp. 1047–1056, Geol. Soc., London.
Klingelhöfer, F., R. A. Edwards, R. W. Hobbs, and R. W. England (2005), Crustal structure of the NE Rockall Trough from wide-angle seismic data modeling, *J. Geophys. Res.*, *110*, B11105, doi:10.1029/2005JB003763.
Korenaga, J., W. S. Holbrook, G. M. Kent, P. B. Kelemen, R. S. Detrick, J. R. Hopper, and T. Dahl-Jensen (2000), Crustal structure of the southeast Greenland margin from joint refraction and reflection seismic tomography, *J. Geophys. Res.*, *105*, 21,591–21,614, doi:10.1029/2000JB900188.
Korenaga, J., P. B. Kelemen, and W. S. Holbrook (2002), Methods for resolving the origin of large igneous provinces from crustal seismology, *J. Geophys. Res.*, *107*(B9), 2178, doi:10.1029/2001JB001030.
Landes, M., J. R. R. Ritter, P. W. Readman, and B. O'Reilly (2005), A review of the Irish crustal structure and signatures from the Caledonian and Variscan orogenies, *Terra Nova*, *17*, 111–120, doi:10.1111/j.1365-3121.2004.00590.x.
Larsen, H. C., and S. Jakobsdottir (1988), Distribution, crustal properties and significance of seaward dipping reflectors off east Greenland, in *Early Tertiary Volcanism and the Opening of the NE Atlantic*, edited by A. C. Morton and L. M. Parson, in *Geol. Soc. Spec. Publ.*, *39*, pp. 95–114.
Larsen, H. C., and A. D. Sauders (1998), Tectonism and volcanism at the southeast Greenland rifted margin: A record of plume impact and later continental rifting, *Proc. Ocean Drill. Program Sci. Results*, *152*, 503–533.
Larsen, H. C., and L. Thorning (1979), Project Eastmar: Acquisition of high sensitivity aeromagnetic data off east Greenland, *Rapp. Groenl. Geol. Unders.*, *100*, 91–94.
Larsen, H. C., et al. (1994a), Introduction: Breakup of the southeast Greenland margin and the formation of the Irminger Basin: Background and scientific objectives, *Proc. Ocean Drill. Program Initial Rep.*, *152*, 5–16.
Larsen, H. C., A. D. Saunders, P. D. Clift, and the Shipboard Scientific Party (1994b), Summary and principal results, *Proc. Ocean Drill. Program Initial Rep.*, *152*, 279–292.
Larsen, H. C., R. A. Duncan, J. F. Allan, and K. Brooks (1999), *Proceedings of the Ocean Drilling Program, Scientific Results*, vol. 163, 269 pp., Ocean Drill. Program, College Station, Tex.
LASE Study Group, (1986), Deep structure of the U.S. East Coast passive margin from large aperture seismic experiments (LASE), *Mar. Geophys. Res.*, *3*, 234–242.
Laughton, A. S., et al. (1972), *Initial Reports of the Deep Sea Drilling Project*, vol. 12, Deep Sea Drill. Proj., Washington, D.C.
Louden, K. E., and D. Chian (1999), The deep structure of non-volcanic rifted continental margins, *Philos. Trans. R. Soc. London, Ser. A*, *357*, 767–804, doi:10.1098/rsta.1999.0352.
Lowe, C., and A. W. B. Jacob (1989), A north-south seismic profile across the Caledonian Suture zone in Ireland, *Tectonophysics*, *168*, 297–318, doi:10.1016/0040-1951(89)90224-2.
Lunnon, Z. C., P. A. F. Christie, and R. S. White (2003), An evaluation of peak and bubble tuning in sub-basalt seismology: Modelling and results from OBS data, *First Break*, *21*(12), 51–56.
Mackenzie, G. D., H. Thybo, and P. K. H. Maguire (2005), Crustal velocity structure across the main Ethiopian rift: Results from two-dimensional wide-angle seismic modelling, *Geophys. J. Int.*, *162*, 994–1006, doi:10.1111/j.1365-246X.2005.02710.x.
Maclennan, J., and B. Lovell (2002), Control of regional sea-level by surface uplift and subsidence caused by magmatic underplating of Earth's crust, *Geology*, *30*, 675–678, doi:10.1130/0091-7613(2002)030<0675:CORSLB>2.0.CO;2.
Maclennan, J., D. P. McKenzie, K. Gronvold, and L. M. Slater (2001), Crustal accretion under northern Iceland, *Earth Planet. Sci. Lett.*, *191*, 295–310, doi:10.1016/S0012-821X(01)00420-4.
Macnab, R., J. Verhoef, W. Roest, and J. Arkani-Hamed (1995), New database documents the magnetic character of the Arctic and North Atlantic, *Eos Trans. AGU*, *76*, 449, 458.
Maresh, J., and R. S. White (2005), Seeing through a glass, darkly: Strategies for imaging through basalt, *First Break*, *23*(1), 27–32.
McBride, J. H., T. J. Henstock, R. S. White, and R. W. Hobbs (1994), Seismic reflection profiling in deep water: Avoiding spurious reflectivity at lower crustal and upper-mantle traveltimes, *Tectonophysics*, *232*, 425–435, doi:10.1016/0040-1951(94)90101-5.
McInroy, D. B., K. Hitchen, and M. S. McInroy (2006), Potential Eocene and Oligocene stratigraphic traps of the Rockall Plateau, NE Atlantic Margin, in *The Deliberate Search for the Stratigraphic Trap*, edited by M. R. Allen, in *Geol. Soc. Spec. Publ.*, *254*, pp. 247–266.
McKenzie, D. (1984), A possible mechanism for epeirogenic uplift, *Nature*, *307*, 616–618, doi:10.1038/307616a0.
Morgan, J. V., P. J. Barton, and R. S. White (1989), The Hatton Bank continental margin–III. Structure from wide-angle OBS and multichannel seismic refraction profiles, *Geophys. J. Int.*, *98*, 367–384, doi:10.1111/j.1365-246X.1989.tb03358.x.
Mutter, J. C., and C. M. Zehnder (1988), Deep crustal structure and magmatic processes: The inception of seafloor spreading in the Norwegian-Greenland Sea, in *Early Tertiary Volcanism and the Opening of the North Atlantic*, edited by A. C. Morton and L. M. Parson, Geol Soc. Spec. Publ., *39*, pp. 35–48.
Mutter, J. C., M. Talwani, and P. L. Stoffa (1982), Origin of seaward dipping reflectors in oceanic crust off the Norwegian margin by "subaerial seafloor spreading", *Geology*, *10*, 353–357, doi:10.1130/0091-7613(1982)10<353:OOSRIO>2.0.CO;2.
Mutter, J. C., M. Talwani, and P. L. Stoffa (1984), Evidence for a thick oceanic crust adjacent to the Norwegian Margin, *J. Geophys. Res.*, *89*, 483–502, doi:10.1029/JB089iB01p00483.
Nielsen, T. K., and J. R. Hopper (2002), Formation of volcanic rifted margins: Are temperature anomalies required?, *Geophys. Res. Lett.*, *29*(21), 2022, doi:10.1029/2002GL015681.
Nielsen, T. K., and J. R. Hopper (2004), From rift to drift: Mantle melting during continental breakup, *Geochem. Geophys. Geosyst.*, *5*, Q07003, doi:10.1029/2003GC000662.
O'Hara, M. (1965), Primary magmas and the origin of basalts, *Scott. J. Geol.*, *1*, 19–40.
Parkin, C. J., and R. S. White (2008), Influence of the Iceland mantle plume on oceanic crust generation in the North Atlantic, *Geophys. J. Int.*, doi:10.1111/j.1365-246X.2007.03689.x.
Putirka, K. (2008), Excess temperatures at ocean islands: Implications for mantle layering and convection, *Geology*, *36*, 283–286, doi:10.1130/G24615A.1.
Roberts, D. G., et al. (1984), *Initial Reports of the Deep Sea Drilling Project*, vol. 81, Deep Sea Drill. Proj, Washington, D.C.
Rowley, E., and N. White (1998), Inverse modelling of extension and denudation in the East Irish Sea and surrounding areas, *Earth Planet. Sci. Lett.*, *161*, 57–71, doi:10.1016/S0012-821X(98)00137-X.
Sallarès, V., P. Charvis, E. R. Flueh, J. Bialas, and the SALIERI Scientific Party (2005), Seismic structure of the Carnegie ridge and the nature of the Galápagos hotspot, *Geophys. J. Int.*, *161*, 763–788, doi:10.1111/j.1365-246X.2005.02592.x.
Sandwell, D. T., and W. H. F. Smith (1997), Marine gravity from Geosat and ERS 1 satellite altimetry, *J. Geophys. Res.*, *102*, 10,039–10,054, doi:10.1029/96JB03223.
Saunders, A D., H. C. Larsen, and S. W. Wise Jr. (1998), *Proceedings of the Ocean Drilling Program, Scientific Results*, vol. 152, Ocean Drill. Program, College Station, Tex.
Sinton, C. W., and R. A. Duncan (1998), $^{40}Ar-^{39}Ar$ ages of lavas from the southeast Greenland margin, ODP Leg 152, and the Rockall Plateau, DSDP Leg 81, *Proc. Ocean Drill. Program, Sci. Results*, *152*, 387–402.
Smallwood, J. R., and R. S. White (2002), Ridge-plume interaction in the North Atlantic and its influence on continental breakup and seafloor spreading, in *The North Atlantic Igneous Province: Stratigraphy, Tectonic, Volcanic and Magmatic Processes*, edited by D. W. Jolley and B. R. Bell, in *Geol. Soc. Spec. Publ.*, *197*, pp. 15–37.
Smallwood, J. R., M. J. Towns, and R. S. White (2001), The structure of the Faroe-Shetland Trough from integrated deep seismic and potential field modelling, *J. Geol. Soc.*, *158*, 409–412.
Smith, L. K., R.S. White, N. J. Kusznir, and iSIMM Team (2005), Mantle plume influence on the Hatton-Rockall Basin and adjacent continental margin, in *Petroleum Geology: North-West Europe and Global Perspectives—Proceedings of the 6th Petroleum Geology Conference*, edited by A. G. Doré and B. A. Vining, pp. 947–956, Geol. Soc., London.
Spence, G. D., R. S. White, G. K. Westbrook, and S. R. Fowler (1989), The Hatton Bank continental margin I. Shallow structure from two-ship expanding spread seismic profiles, *Geophys. J. Int.*, *96*, 273–294, doi:10.1111/j.1365-246X.1989.tb04451.x.
Tarantola, A. (1987), *Inverse Problem Theory and Methods for Model Parameter Estimation*, Elsevier Sci., New York.
Tegner, C., R. A. Duncan, and R. A. Duncan (1999), $^{40}Ar-^{39}Ar$ chronology for the volcanic history of the southeast Greenland rifted margin, *Proc. Ocean Drill. Program, Sci. Results*, *163*, 53–62.
Thompson, R. N. (1974), Primary basalts and magma genesis, I, Skye, north-west Scotland, *Contrib. Mineral. Petrol.*, *45*, 317–341, doi:10.1007/BF00371750.

Thompson, R. N., A. J. V. Riches, P. M. Antoshechkina, D. G. Pearson, G. M. Nowell, C. J. Ottley, A. P. Dickin, V. L. Hards, A.-K. Nguno, and V. Niku-Paavola (2007), Origin of CFB magmatism: Multi-tiered intracrustal picrite-rhyolite magmatic plumbing at Spitzkoppe, western Namibia, during early Cretaceous Etendeka magmatism, *J. Petrol.*, *48*, 1119–1154, doi:10.1093/petrology/egm012.

Vogt, U., J. Makris, B. M. O'Reilly, F. Hauser, P. W. Readman, A. W. B. Jacob, and P. M. Shannon (1998), The Hatton Basin and continental margin: Crustal structure from wide-angle seismic and gravity data, *J. Geophys. Res.*, *103*, 12,545–12,566, doi:10.1029/98JB00604.

Voss, M., and W. Jokat (2007), Continent-ocean transition and voluminous magmatic underplating derived from P wave velocity modelling of the east Greenland continental margin, *Geophys. J. Int.*, *170*, 580–604, doi:10.1111/j.1365-246X.2007.03438.x.

White, N., and B. Lovell (1997), Measuring the pulse of a plume with the sedimentary record, *Nature*, *387*, 888–891, doi:10.1038/43151.

White, R. S. (1987), When continents rift, *Nature*, *327*, 191, doi:10.1098/rsta.1997.0011.

White, R. S. (1997), Rift-plume interaction in the North Atlantic, *Philos. Trans. R. Soc. London, Ser. A*, *355*, 319–339, doi:10.1098/rsta.1997.0011.

White, R., and D. McKenzie (1989), Magmatism at rift zones: The generation of volcanic continental margins and flood basalts, *J. Geophys. Res.*, *94*, 7685–7729, doi:10.1029/JB094iB06p07685.

White, R. S., and D. McKrnzie (1995), Mantle plumes and flood basalts, *J. Geophys. Res.*, *100*, 17,543–17,585, doi:10.1029/95JB01585.

White, R. S., G. D. Spence, S. R. Fowler, D. P. McKenzie, G. K. Westbrook, and A. N. Bowen (1987), Magmatism at rifted continental margins, *Nature*, *330*, 439–444, doi:10.1038/330439a0.

White, R. S., D. White, and R. K. O'Nions (1992), Oceanic crustal thickness from seismic measurements and rare earth element inversions, *J. Geophys. Res.*, *97*, 19,683–19,715, doi:10.1029/92JB01749.

White, R. S., et al. (2002), iSIMM pushes frontiers of marine seismic acquisition, *First Break*, *20*(12), 782–786.

White, R. S., L. K. Smith, A. W. Roberts, F. Christie, N. J. Kusznir, and iSIMM Team (2008), Lower-crustal intrusion on the North Atlantic continental margin, *Nature*, *452*, 460–464, doi:10.1038/nature06687.

Zelt, C. A., and P. J. Barton (1998), Three-dimensional seismic refraction tomography: A comparison of two methods applied to data from the Faeroe basin, *J. Geophys. Res.*, *103*(B4), 7187–7210, doi:10.1029/97JB03536.

Zelt, C. A., and R. B. Smith (1992), Seismic travel time inversion for 2-D crustal velocity structure, Geophys, *J. Int.*, *108*, 16–24, doi:10.1111/j.1365-246X.1992.tb00836.x.

Zhang, A., and M. N. Toksöz (1998), Nonlinear refraction traveltime tomography, *Geophysics*, *63*, 1726–1737, doi:10.1190/1.1444468.

L. K. Smith, BP, Burnside Road, Farburn Industrial Estate, Dyce, Aberdeen AB21 7PB, UK.

R. S. White, Bullard Labs, Madingley Road, Cambridge CB3 0EZ, UK. (rsw1@cam.ac.uk)